

Implications for Galaxy Formation Models from Observations of Globular Clusters around Ultra-Diffuse Galaxies

Teymoor Saifollahi^{1*}, Dennis Zaritsky², Ignacio Trujillo^{3,4}, Reynier F. Peletier¹, Johan H. Knapen^{3,4}, Nicola Amorisco⁵, Michael A. Beasley^{3,4}, Richard Donnerstein²

¹*Kapteyn Astronomical Institute, University of Groningen, PO Box 800, 9700 AV Groningen, The Netherlands*

²*Steward Observatory, University of Arizona, Tucson, AZ 85719, USA*

³*Instituto de Astrofísica de Canarias, Vía Láctea S/N, E-38205 La Laguna, Spain*

⁴*Departamento de Astrofísica, Universidad de La Laguna, E-38206 La Laguna, Spain*

⁵*Institute for Computational Cosmology, Department of Physics, Durham University, South Road, Durham DH1 3LE, UK*

Accepted XXX. Received YYY; in original form ZZZ

ABSTRACT

We present an analysis of *Hubble Space Telescope* observations of globular clusters (GCs) in six ultra-diffuse galaxies (UDGs) in the Coma cluster, a sample that represents UDGs with large effective radii (R_e), and use the results to evaluate competing formation models. We eliminate two significant sources of systematic uncertainty in the determination of the number of GCs, N_{GC} by using sufficiently deep observations that (i) reach the turnover of the GC luminosity function and (ii) provide a sufficient number of GCs with which to measure the GC number radial distribution. We find that N_{GC} for these galaxies is on average ~ 20 , which implies an average total mass, M_{total} , $\sim 10^{11} M_\odot$ when applying the relation between N_{GC} and M_{total} . This value of N_{GC} lies at the upper end of the range observed for dwarf galaxies of the same stellar mass and is roughly a factor of two larger than the mean. The GC luminosity function, radial profile and average colour are more consistent with those observed for dwarf galaxies than with those observed for the more massive (L^*) galaxies, while both the radial and azimuthal GC distributions closely follow those of the stars in the host galaxy. Finally, we discuss why our observations, specifically the GC number and GC distribution around these six UDGs, pose challenges for several of the currently favoured UDG formation models.

Key words: galaxies: clusters: individual (Coma) - galaxies: evolution - galaxies: structure - dark matter

1 INTRODUCTION

The increasing depth of astronomical surveys continues to reveal the existence of ever lower surface brightness galaxies (Binggeli et al. 1985; Bothun et al. 1991; Impey & Bothun 1997; van Dokkum et al. 2015a; Fliri & Trujillo 2016; Trujillo et al. 2021), which due to their extreme nature can challenge galaxy formation models. In particular, a subclass of low surface brightness (LSB) galaxies with large effective radii ($R_e > 1.5$ kpc) and low surface brightness ($\mu_{(0,g)} > 24.0$ mag arcsec⁻²), dubbed ultra-diffuse galaxies (UDGs) by van Dokkum et al. (2015a), has drawn attention both because of their large numbers and inferred properties.

The large population of UDGs in Coma and their survival in the cluster environment suggested large total masses, M_{total} , despite their modest stellar masses (van Dokkum et al. 2015a). Further investigations and estimations of the total mass of UDGs using stellar kinematics (van Dokkum et al. 2019; Chilingarian et al. 2019; Müller et al. 2020; Gannon et al. 2020; Forbes et al. 2021), globular clusters (GCs) dynamics (Beasley et al. 2016; Toloba et al. 2018), HI kinematics (Trujillo et al. 2017; Leisman et al. 2017; Papastergis et al. 2017; Mancera Piña et al. 2020; Poulain et al. 2021), weak

gravitational lensing (Sifón et al. 2018), UDG abundance in clusters (Amorisco 2018), scaling relations (Zaritsky 2017), and X-ray observations (Lee et al. 2020) found that most UDGs are dark matter dominated objects with halo masses similar to those of dwarf galaxies and dynamical mass-to-light ratios that span a wide range between a few tens to a few thousands. The most massive known UDGs have $M_{total} \sim 10^{11} M_\odot$, comparable to the most massive dwarf galaxies, such as the LMC (Erkal et al. 2019).

Because of the difficulty in obtaining direct mass estimates of UDGs, some authors have resorted to using the number of globular clusters, N_{GC} , as a secondary mass estimator (Harris et al. 2013; Beasley et al. 2016; Harris et al. 2017) for UDGs in the Coma (Beasley & Trujillo 2016; Peng & Lim 2016; Amorisco et al. 2018; Lim et al. 2018), Virgo (Lim et al. 2020), Fornax (Prole et al. 2018), and Hydra (Iodice et al. 2020) clusters and in galaxy groups (Somalwar et al. 2020; Müller et al. 2021). These observations have highlighted that UDGs tend to host two to three times as many GCs as dwarf galaxies of the same stellar mass (Lim et al. 2018, 2020, but see Amorisco et al. 2018; Prole et al. 2019; Marleau et al. 2021 for multiple counter-examples). Overall, it seems that UDGs show a wide range of GC abundances; some are GC-poor and some are GC-rich (Gannon et al. 2021)

In contrast to GC abundances, other GC properties appear to be

* E-mail: teymur.saif@gmail.com

similar in UDGs and non-UDGs. The ratio of the GC half-number radius (R_{GC}) to the UDG effective radius (R_e) of < 2 , the GC colours (dominantly blue and metal-poor), and the shape of GC luminosity function (GCLF) are all similar to what is found for GCs in dwarf galaxies (Beasley & Trujillo 2016; Peng & Lim 2016; van Dokkum et al. 2017; Amorisco et al. 2018; Prole et al. 2019; Lim et al. 2020; Somalwar et al. 2020; Saifollahi et al. 2021; Müller et al. 2021)

These results suggest that GCs in UDGs are similar to those in other galaxies and that what differs between GCs in UDGs and other galaxies is simply the relative formation efficiency between them and the stars in the host galaxy. As such, GCs may provide an avenue for discriminating among competing UDG formation/evolution models. We briefly outline some competing models and how N_{GC} might be expected to behave:

- The initial UDG studies suggested that UDGs represent a population of failed galaxies that assembled their dark matter haloes and were rapidly quenched at high redshift due to environmental processes in galaxy clusters, mainly ram pressure stripping (van Dokkum et al. 2015a; Koda et al. 2015; Yozin & Bekki 2015; Benavides et al. 2021). Additionally, as a consequence of the passive evolution of their stellar populations, UDGs surface brightness have decreased with time (Román & Trujillo 2017; Román et al. 2019; Tremmel et al. 2020). This scenario is consistent with observations of cluster UDGs as gas-poor (Karunakaran et al. 2020; Chen et al. 2020) quiescent (Singh et al. 2019), old, metal-poor, and alpha-enhanced (Kadowaki et al. 2017; Gu et al. 2018; Pandya et al. 2018; Ruiz-Lara et al. 2018; Ferré-Mateu et al. 2018). This model stemmed from the idea that UDGs are massive objects with L^* -like haloes (van Dokkum et al. 2015a). However, recently this model is revised to accommodate the dwarf-like haloes of UDGs (Beasley et al. 2016; Beasley & Trujillo 2016). In this "failed dwarf galaxy" model, the low surface brightness is attributed to the lack of subsequent star formation, and so naturally results in a larger N_{GC}/M_* , as long as GC formation occurred prior to the introduction of the UDG progenitor into the cluster environment.

- Another environment-motivated class of model, the "tidal interaction" scenario, has UDGs suffering dynamical heating within galaxy clusters and galaxy groups that "puffs" them up (e.g., Carleton et al. 2019; Amorisco 2019; Sales et al. 2020). Studies exist that both favour (Mancera Piña et al. 2019; Rong et al. 2020; Jones et al. 2021; Román et al. 2021) or disfavour (Venholá et al. 2017; Kado-Fong et al. 2021) this scenario. In such a scenario, the galaxy's low surface brightness is attributed to the dynamical expansion of the galaxy, not to a lower star formation efficiency, and so N_{GC}/M_* should be comparable to that of dwarf galaxies. If only some UDGs form via this channel, we might expect to find large scatter in N_{GC}/M_* .

- The presence of UDGs in the field ((Prole et al. 2021)) suggests that environment alone is not responsible for UDG formation. In the "high-spin" model (Amorisco & Loeb 2016), a higher initial halo spin for a dwarf-like halo produces a galaxy with a large effective radius and hence low surface brightness. Again, current observations, in this case HI observations of gas-rich UDGs, provide conflicting results with some finding high-spin (Spekkens & Karunakaran 2018; Liao et al. 2019) and others finding low-spin (Jones et al. 2018; Sengupta et al. 2019) field UDGs. In the high-spin UDGs, the baryons are less concentrated than in the low-spin analogs and so, in addition to the stars being more spread out, a lower star formation efficiency may also plausibly be responsible

for the galaxy's low surface brightness. It is unclear whether one would also expect GC formation to have been affected and so the expectations for N_{GC}/M_* are unclear.

- Alternatively, the "stellar feedback" model (Di Cintio et al. 2017) invokes episodic and intense star formation activity in gas-rich galaxies to push the gas to larger radii. In a variant of this model, feedback from the GCs themselves is invoked by Trujillo-Gomez et al. (2022). The redistribution of the gas, which is the dominant baryonic mass component in these galaxies, modifies the total mass distribution within the galaxy, causing the formation of a dark matter core (Navarro et al. 1996; Pontzen & Governato 2012) and lowering the surface brightness (Di Cintio et al. 2017; Jiang et al. 2019; Chan et al. 2018; Martin et al. 2019; Freundlich et al. 2020). As star formation occurs after GC formation, one might expect different radial distributions for GCs and stars. Interestingly, in the model variant where GCs are responsible for the intense feedback (Trujillo-Gomez et al. 2022), we might expect a relation between N_{GC}/M_* and R_e .

- Other models rely on distinctive merger histories to produce a range of surface brightness among otherwise similar galaxies. The "lack of mergers" scenario (Wright et al. 2021; Van Nest et al. 2021) suggests that UDGs are those galaxies with no late-time ($z < 1$) major mergers. In this case, the spin parameter of the galaxy is systematically higher than in analogs that did have such a merger and in turn star formation occurs at larger radii, which leads to a lower central surface brightness. If mergers play a role in GC formation, then N_{GC}/M_* might actually be expected to be lower than in analogs. However, if GCs form only at high redshift, then N_{GC}/M_* might be larger in UDGs.

Each of these proposed mechanisms do not necessarily act at the exclusion of others. For example, Martin et al. (2019) propose that a combination of a distinctive star formation history and environmental effects produces large, low surface brightness galaxies. Even without this additional complication, it is evident from this discussion that theoretical expectations for the number and properties of GCs in the various UDG formation/evolution models need further development. Fortunately, some studies have begun this exploration in detail for specific models (Carleton et al. 2021). Our goal here is to motivate further work by providing higher fidelity GC observations against which to do the comparison.

We address three specific shortcomings of the available N_{GC} measurements. First, and foremost, we provide a consistent analysis of a significant sample (six) of similar UDGs. Second, we focus on a population of large UDGs, $3 < R_e/\text{kpc} < 5$, with a mean effective radius of $\langle R_e \rangle = 3.6$ kpc. These are expected to be more massive and, therefore, to each have a significant number of GCs. Third, we use images that are sufficiently deep to allow us to address two key sources of systematic uncertainty. Every estimate of N_{GC} for UDGs includes completeness corrections, both for GCs too faint to detect and for radial incompleteness due to highly uncertain statistical background corrections at large radii. Our photometry reaches the GCLF turnover, minimizing the photometric completeness correction. Furthermore, we detect a sufficient number of GCs per galaxy, which allows us to empirically constrain the GC radial distribution.

The structure of the paper is as follows. In Section 2, the UDG sample and the observational data are described. In Section 3, after source extraction and photometry, we measure the compactness and colours of sources and identify the GCs around our UDGs. Section 4 presents the observed properties of the identified GCs, their total

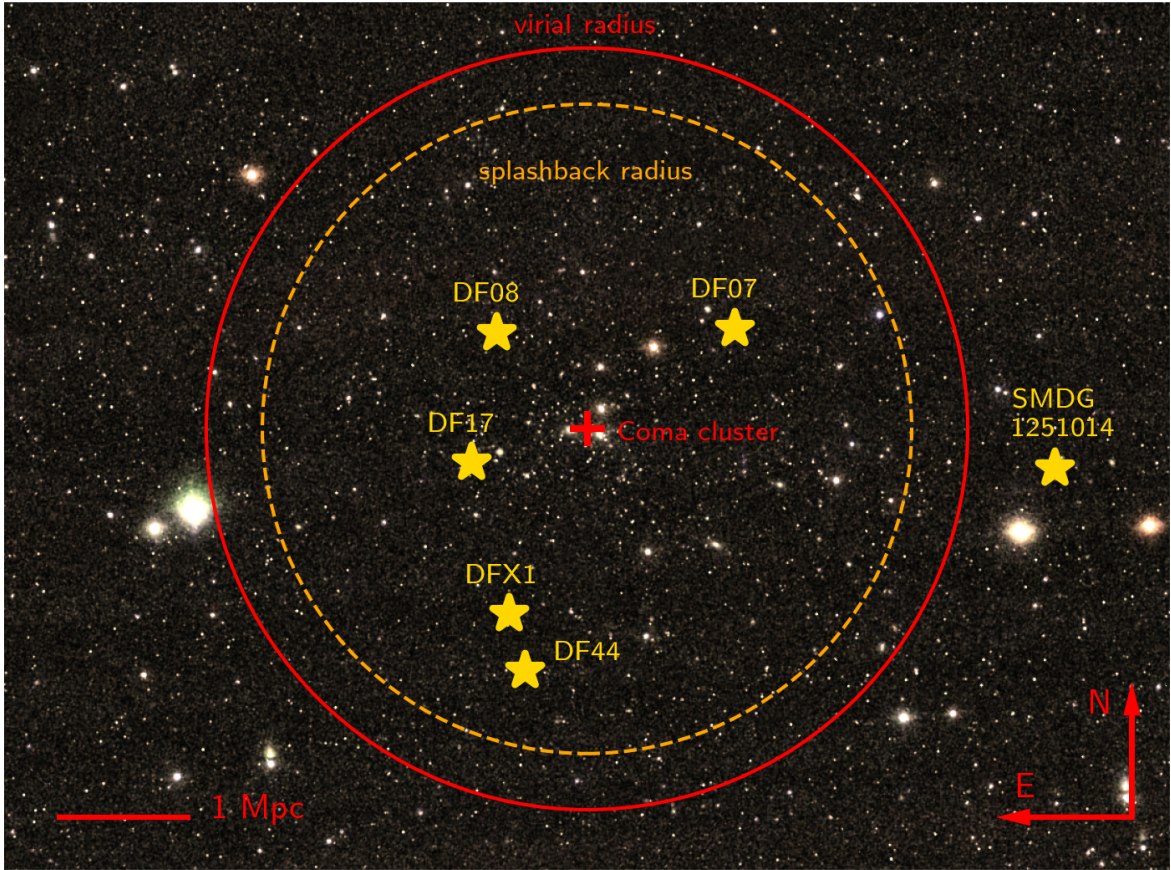


Figure 1. Projected distribution of the six Coma cluster UDGs in this study (colour image: Sloan Digital Sky Survey DR9).

number, spatial distribution, colours and luminosity function. Based on these results, in Section 5 we discuss the implications for various UDG formation scenarios. We summarize our findings in Section 6. Throughout this paper, magnitudes and colours are expressed in the AB magnitude system. We adopt the standard cosmological model with $\Omega_M = 0.3$, $\Omega_\Lambda = 0.7$ and $H_0 = 70 \text{ km s}^{-1} \text{ Mpc}^{-1}$.

2 OBSERVATIONS

2.1 UDG sample

The UDGs in our sample are Coma cluster galaxies with an available spectroscopic redshift, a large effective radius ($R_e \sim 4 \text{ kpc}$), and deep *HST* observations that reach the GCLF turn-over magnitude ($\mu_{\text{peak}} \sim -8.0 \text{ mag}$ in the *I*-band). These criteria narrow down the sample to six UDGs in the Coma cluster with an average effective radius, R_e , of $\sim 3.6 \text{ kpc}$. The Coma cluster is at a distance of 100 Mpc (Thomsen et al. 1997; Jensen et al. 1999)¹ and has a mass of $M_{200} = 1.3 \times 10^{15} M_\odot$, making it one of the most massive galaxy clusters in the local universe (Kubo et al. 2007).

These six galaxies are drawn from previous Coma cluster UDG surveys (van Dokkum et al. 2015a; Yagi et al. 2016; Zaritsky et al. 2019) and, therefore, are known by multiple names. Five of these UDGs have DF names (Dragonfly Coma cluster survey, van Dokkum et al.

2015a) namely, DF07, DF08, DF17, DF44 and DFX1². For convenience, throughout this paper, we use the DF names for these five galaxies, although they all appear in both the Yagi et al. (2016) and Zaritsky et al. (2019) catalogs as well. The sixth galaxy, known as SMDG1251014+274753 (hereafter we refer to this object as SMDG1251014) is identified by the SMUDGes survey of the Coma cluster (Zaritsky et al. 2019; Barbosa et al. 2020; Zaritsky et al. 2021). The UDG sample is presented in Table 1 and their distribution relative to the Coma cluster is shown in Fig. 1. The Coma membership of these objects is spectroscopically confirmed (van Dokkum et al. 2015b, 2016, 2017; Kadowaki et al. 2017; Gu et al. 2018; Kadowaki et al. 2021). All, except SMDG1251014 are located within the virial radius (2.85 Mpc, Kubo et al. 2007) and the splashback radius of the cluster (2.43 Mpc, Kadowaki et al. 2021; Diemer 2018).

2.2 Photometric data

Our data come from three different programs carried out with the *Hubble Space Telescope* (*HST*). The first (*HST* program ID 15121; PI Zaritsky) provides WFC/ACS *F475W* and *F814W* observations of DF07, DF08, DF44 and SMDG1251014. These observations were defined to deliver similar data to those available for DF17 from the

² This galaxy, which was originally named "GMP 2175" (Godwin et al. 1983), is not included in the main DF catalogue (van Dokkum et al. 2015a) but was added later, in van Dokkum et al. (2017), and renamed DFX1.

¹ Radial velocity of 6925 km/s (Struble & Rood 1999).

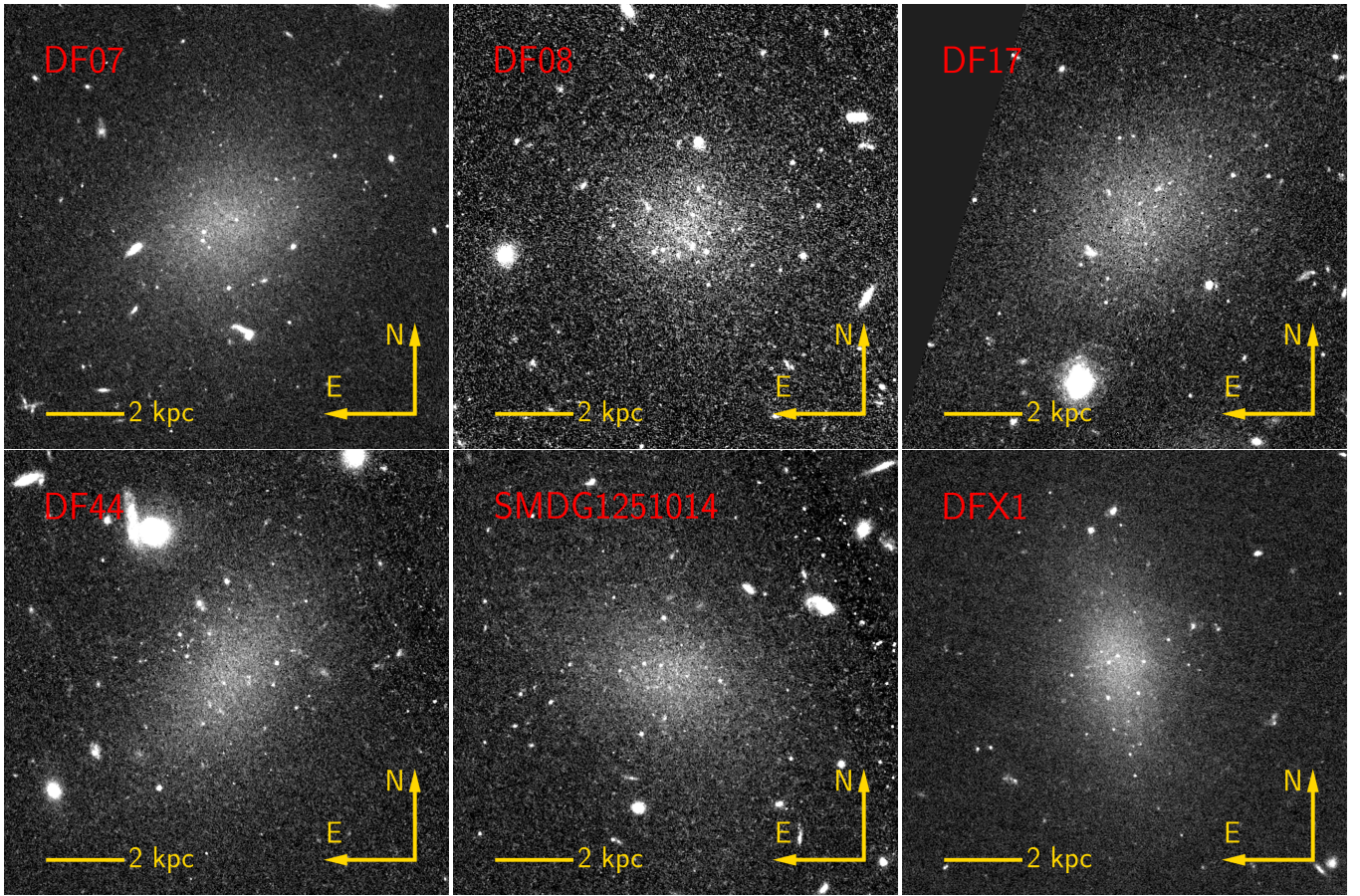


Figure 2. The WFC/ACS/HST view of the UDG sample of this work in $F814W$ for DF07, DF08, DF17, DF44, SMDG1251014 and $F606W$ for DFX1.

Table 1. The UDG sample and the observational data of this work. Columns from left to right represent galaxy names in the SMUDGes (Zaritsky et al. 2019) and Yagi (Yagi et al. 2016) catalogs (a), R.A. (b), Declination (c), heliocentric radial velocity (d) and exposure times in three filters, $F475W$, $F606W$, $F814W$, for available data (e, f and g). The * and ** symbols indicate the primary and secondary datasets, respectively. For convenience, throughout this paper, we use the DF name for five galaxies and the SMDG name for one galaxy. These names are indicated in boldface.

Names (SMDG,DF,Yagi) (a)	J2000 RA (deg) (b)	J2000 DEC (deg) (c)	V_{rad} (km/s) (d)	$F475W$ (e)	$F606W$ (f)	$F814W$ (g)
SMDG1257017+282325, DF07 , 680	194.25716	28.390250	$6,864 \pm 33$	5,000s**	—	5,000s*
SMDG1301304+282228, DF08 , 194	195.37646	28.374578	$7,319 \pm 97$	5,000s**	—	5,000s*
SMDG1301582+275011, DF17 , 165	195.49266	27.836445	$8,583 \pm 43$	5,100s**	5,800s	5,100s*
SMDG1300580+265835, DF44 , 11	195.24162	26.976355	$6,661 \pm 38$	5,000s**	7,280s	5,000s*
SMDG1251014+274753 , —, —	192.75563	27.798033	$6,404 \pm 45$	5,000s**	—	3,730s*
SMDG1301158+271238, DFX1 , 13	195.31600	27.210484	$8,105 \pm 6$	—	7,280 s*	2,420s**

second program (*HST* program ID 12476; PI Cook). This program provides WFC/ACS observations in $F475W$, $F606W$ and $F814W$, which has been used previously (Beasley & Trujillo 2016; Peng & Lim 2016). The final program (*HST* program ID 14643; PI van Dokkum) provides WFC3/UVIS $F606W$ and $F814W$ observations of DFX1 and DF44. These data have been also used previously (van Dokkum et al. 2017; Saifollahi et al. 2021). However, the $F814W$ observations of DF44 are shallower than our $F814W$ so we do not use them here. In Table 1 we summarize the observations and basic properties (coordinates and recessional velocity) of our UDGs.

We retrieve the reduced data from the MAST server³. When more than one frame for a given filter is available, we median stack the frames using SWARP (Bertin et al. 2002). We remove cosmic rays from the stacked frames using the L.A.Cosmic⁴ (van Dokkum 2001). These processed frames, with cropped versions shown in Fig. 2, are used in the next section to measure the Sérsic parameters of galaxies, perform photometry and select GC candidates. For each galaxy, we

³ All data are now public and accessible via <https://mast.stsci.edu/portal/Mashup/Clients/Mast/Portal.html>

⁴ L.A.Cosmic PYTHON package is available here: <https://lacosmic.readthedocs.io/en/latest/>

select the image that has the highest signal-to-noise ratio as the primary frame that we will use as a reference. For all except DFX1, the *F814W* images are defined as primary. For DFX1, the *F606W* images is defined as the primary.

3 ANALYSIS

We use the primary and secondary images to measure the structural properties of UDGs, extract sources and ultimately, identify the globular clusters. In this section, we describe our methodology.

3.1 Galaxy structural parameters

To derive the structural properties of the UDGs, we fit a single Sérsic function using GALFIT (Peng et al. 2002, 2010) to the 32×32 arcsec (16×16 kpc) cropped images. This crop size covers beyond $2R_e$ for all of our UDGs. To estimate the background flux, we make larger cropped frames of galaxies (80×80 arcsec or 40×40 kpc). Bright contaminating objects in the images are extracted using SExtractor (Bertin & Arnouts 1996) with the default parameters except that we set BACK_TYPE=GLOBAL, BACK_SIZE=16, and BACK_FILTERSIZE=1. We find that this configuration extracts sources located within the galaxy more effectively. At this point, we aim to identify bright sources that may influence the model fitting. Later, for GC identification, we will use a more sophisticated background subtraction (described in Section 3.2).

To determine the background level, we place a circular mask with a radius of 10 times the estimated minor axis (SExtractor output *B_IMAGE*) for each source other than the UDG and a square mask of 32 arcsec on a side for the UDG. We calculate the sigma-clipped median of the sky values (5 iterations with 3σ clipping) for 1,000 randomly placed 5×5 arcsec (100×100 pixel) boxes. Finally, the median of these median values is used as the background flux input to GALFIT, which floats during fitting. Figures A1 and A2 in the appendix display the different steps of the Sérsic modeling.

We present in Table 2 the resulting Sérsic parameters for the galaxies and show the surface brightness profiles and fits in Fig. 3 for DF44 and in Figure A3 for the rest of the sample. In the cases where the same images are used, our derived values for the effective radii, R_e , are consistent with previous measurements (van Dokkum et al. 2015a; Peng & Lim 2016; Beasley & Trujillo 2016 for DF17; van Dokkum et al. 2017 for DFX1; Saifollahi et al. 2021 for DF44). For DF44, using the *HST* data in *F606W*, van Dokkum et al. 2017 measured an R_e that is on average ~ 0.8 kpc larger than our measurements in any of the three available filters. A possible explanation for this difference lies in the estimation of the background level, which can lead to different Sérsic indices and ultimately, different effective radii.

3.2 Source extraction and photometry

We perform source extraction and source photometry using SExtractor to construct the source catalogue that is needed for the next steps in our analysis. To improve the source extraction, we subtract an 8×8 pixel (spatial) median-filter from each frame. We identify and extract sources using SExtractor and its default parameters. Detected sources are masked and the procedure (filtering, source extraction, masking) is repeated three more times. The final median-subtracted frames are used to construct the source catalogues. For this search we use the default SExtractor values with a few adjustments: DETECT_MINAREA=4.0, DETECT_THRESH=1.5,

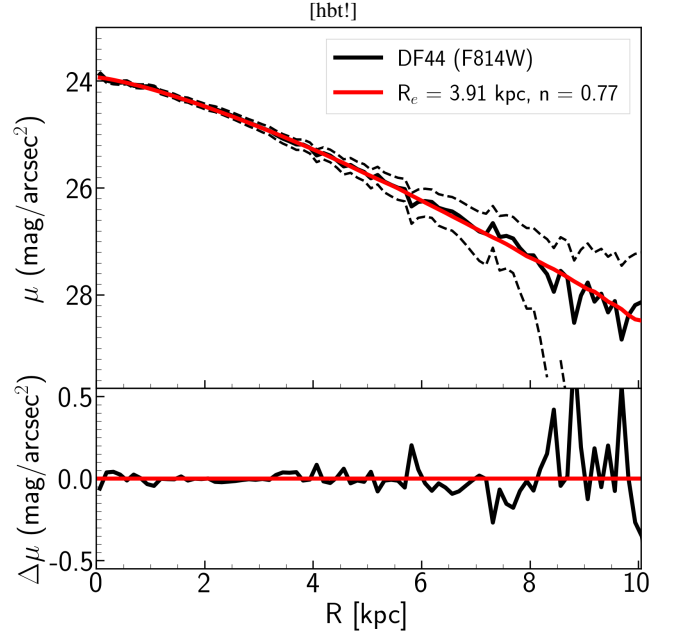


Figure 3. The light profile (solid black lines), best-fit Sérsic function (red curve) for the UDG DF44 (top) and fitting residuals (bottom). The black dashed lines indicate the 1-sigma uncertainty of the light profile.

ANALYSIS_THRESH=1.5, DEBLEND_NTHRESH=4, DEBLEND_MINCONT=0.005, BACK_TYPE=GLOBAL, BACK_SIZE=32, and BACK_FILTERSIZE=3. We calculate aperture magnitudes within apertures of 4 and 8 pixel diameter. We use the 4 pixels aperture magnitudes ($\sim 2 \times$ FWHM) to measure the source aperture magnitude and, in combination with the 8 pixel aperture magnitudes, to measure a source compactness index. The aperture corrections we apply are as presented in the instrument handbook and are 0.44, 0.45 and 0.54 mag for *F475W*, *F606W* and *F814W* respectively. We adopt zeropoints from the ACS Zeropoints calculator⁵. These values are slightly different between observations that have been carried out at different times.

3.3 Identifying GC candidates

Here we describe how we identify GC candidates. Because ACS has a pixel size of 0.05 arcsec and the point spread function full width half maximum (FWHM) is 0.1 arcsec (2 pixels), this instrument is the best available for GC searches in UDGs at distances between that of the Virgo and Coma clusters. Although GCs are unresolved in the *HST* observations of systems at the distance of the Coma cluster (Harris et al. 2009), the high-resolution imaging of the ACS can distinguish them from high-redshift background galaxies, which are resolved. Furthermore, the 202×202 arcsec field of view compares well to the average effective radius of UDGs in the sample (7.2 arcsec on average), providing enough field coverage to allow us to statistically estimate any remaining contamination after the source selection procedure described below.

As already indicated, GCs at the Coma distance are unresolved. To help distinguish them from background galaxies, we define a compactness index, c_{4-8} , as the difference between the 4 and 8 pixels

⁵ <https://acszeropoints.stsci.edu/>

Table 2. UDG structural parameters of our UDGs. Columns from left to right represent (a) galaxy name as referred to in this work, (b) observed filter, (c) effective radius, (d) Sérsic index, (e) major axis position angle measured counterclockwise from North to East, (f) ellipticity, (g) total apparent magnitude, (h) total absolute magnitude, (i) effective surface brightness, (j) and the inferred stellar mass. The * and ** symbols denote the primary and secondary datasets. Absolute magnitudes are calculated using an adopted distance modulus $m - M = 35$, assuming that all Coma galaxies are at 100 Mpc. Uncertainties come from the model fitting using GALFIT. The stellar masses are estimated using the equations in [Into & Portinari \(2013\)](#) after converting M_{814} , $m_{475} - m_{814}$, and $m_{606} - m_{814}$ to I , $B - I$ and $V - I$. The conversion are made using $m_{V, \text{Vega}} - m_{I, \text{Vega}} = m_{606, \text{AB}} - m_{814, \text{AB}} + 0.58$ and $m_{B, \text{Vega}} - m_{I, \text{Vega}} = m_{475, \text{AB}} - m_{814, \text{AB}} + 0.82$ ([Blanton & Roweis 2007](#); [Gennaro, M., et al. 2018](#); [Harris 2018](#)). Systematic magnitude errors are small in comparison to the uncertainties in model fitting and neglected.

Galaxy	Filter	R_e kpc	n	PA deg	ϵ	m mag	M mag	$\langle \mu_e \rangle$ mag/arcsec ²	M_* $10^8 M_\odot$
(a)	(b)	(c)	(d)	(e)	(f)	(g)	(h)	(i)	(j)
DF07	<i>F475W</i> **	3.74±0.37	0.85±0.08	-46.5±0.63	0.77±0.01	19.38±0.15	-15.61±0.15	25.74±0.36	2.8±0.7
	<i>F814W</i> *	3.55±0.04	0.81±0.01	-45.9±0.04	0.79±0.01	18.45±0.02	-16.54±0.02	24.69±0.04	
DF08	<i>F475W</i> **	3.07±0.86	1.03±0.22	-81.6±1.29	0.99±0.01	20.65±0.35	-14.34±0.35	26.58±0.95	0.6±0.2
	<i>F814W</i> *	2.95±0.17	0.88±0.05	70.13±0.31	0.90±0.01	19.77±0.09	-15.22±0.09	25.61±0.21	
DF17	<i>F475W</i> **	3.75±0.35	0.71±0.08	-48.0±0.77	0.75±0.01	20.00±0.16	-14.99±0.16	26.36±0.36	1.4±0.4
	<i>F606W</i>	3.48±0.20	0.65±0.04	-53.5±0.13	0.73±0.01	19.66±0.10	-15.33±0.10	25.86±0.22	
	<i>F814W</i> *	3.45±0.20	0.65±0.04	-49.7±0.31	0.73±0.01	19.16±0.10	-15.83±0.10	25.34±0.22	
DF44	<i>F475W</i> **	4.21±0.61	0.77±0.11	-20.1±1.25	0.67±0.01	19.39±0.24	-15.60±0.24	26.01±0.55	2.1±0.5
	<i>F606W</i>	3.83±0.40	0.74±0.09	-29.2±0.46	0.64±0.01	19.19±0.17	-15.80±0.17	25.60±0.40	
	<i>F814W</i> *	3.92±0.01	0.77±0.01	-24.4±0.03	0.68±0.01	18.62±0.01	-16.37±0.01	25.08±0.01	
SMDG1251014	<i>F475W</i> **	5.06±0.80	0.94±0.11	49.25±0.88	0.71±0.01	19.16±0.24	-15.83±0.24	26.17±0.58	4.9±1.2
	<i>F814W</i> *	4.99±0.29	1.01±0.04	50.03±0.40	0.74±0.01	18.22±0.09	-16.77±0.09	25.20±0.20	
DFX1	<i>F606W</i> *	3.73±0.17	0.93±0.04	9.85±0.05	0.60±0.01	19.18±0.07	-15.81±0.07	25.53±0.16	1.5±0.4
	<i>F814W</i> **	3.69±0.22	0.92±0.05	10.86±0.22	0.59±0.01	18.77±0.09	-16.22±0.09	25.10±0.21	

aperture magnitudes. Because the primary frames were selected to have a higher signal-to-noise ratio, we adopt the c_{4-8} measured from those. In the following, we select point sources as GC candidates based on this compactness criteria. We then use the measured colours to further clean the sample of possible contamination (foreground/background). Next, we describe each step in detail.

3.3.1 Artificial stars and point source selection

GC candidate selection based on the compactness index is a well-established approach (e.g. [Jordán et al. 2007, 2015](#); [Amorisco et al. 2018](#); [Lim et al. 2018](#)). The compactness index threshold is established for each different data set through comparisons of the resulting compactness indices of implanted artificial stars. The point spread function (PSF) used to create those stars is typically determined using bright and unsaturated stars in the data.

To implant artificial stars, we first discard all objects brighter than 22nd magnitude because these are ~ 5 mag brighter than the expected GCLF peak. Assuming a GCLF width of $\sigma = 1.0$ mag ([Brodie & Strader 2006](#)), this limit is $\sim 5\sigma$ from the GCLF peak. We conclude that compact objects brighter than 22 mag are foreground stars. From the remaining sources, we select between 10 and 20 of the brightest unsaturated stars in each primary frame. These are brighter than 25 mag in *F814W* and with a compactness index between 0.25 and 0.45 mag. This range of compactness index is chosen by visual inspection of the compactness index - magnitude diagram of sources. After selecting stars within primary frames, we re-sample their PSFs at a pixel size 10 times smaller, combine all of the PSFs, and re-construct the PSF of each primary frame. The reconstructed PSFs have a pixel size of 0.005 arcsec. Given the small number of bright unsaturated stars in each frame, we choose to adopt a constant PSF across the frame.

We simulate 1,000 stars with magnitudes between 22 and 29 mag per 0.1 mag bin. We randomly locate artificial stars to sub-pixel precision (along X-axis and Y-axis, within 10 pixels from the PSF centroid), re-sample to the instrumental pixel size (0.05 arcsec), add Poisson noise, and randomly distribute them throughout the original images.

For each of the new images produced, we perform cosmic ray rejection, source extraction and photometry as we did before. In Fig. 4 we show the c_{4-8} - magnitude diagram of the simulated stars for DF44 (the diagrams for the other galaxies are in Fig. A5). Based on the median and standard deviation of c_{4-8} at each magnitude, we define a range of c_{4-8} as characteristic of point sources (indicated by black dashed curves) and select objects within these curves as GC candidates (red crosses). The boundaries correspond to 3σ deviations from the median compactness index of the artificial stars plus 0.1 mag to account for compactness variations across a frame.

Using the artificial star results we estimate that we are 90 per cent complete in identifying point sources near the expected GCLF turnover (27.8 and 27.3 mag in *F606W* and *F814W*). The full completeness function is presented in Fig. 5 for DF44 and Fig. A8 for the other UDGs.

3.3.2 Colour-based selection

Following the point source selection using the primary image, we use the secondary data to apply a colour cut. Requiring a positional match in the secondary image (within 0.1 arcsec or 2 pixels) rejects most remaining cosmic rays. Unfortunately, some cosmic rays, regardless of the cosmic ray cleaning and compactness criteria, remain and make their way into the sample of selected point sources. We will account for these and other remaining contaminants statistically in the next steps of the analysis.

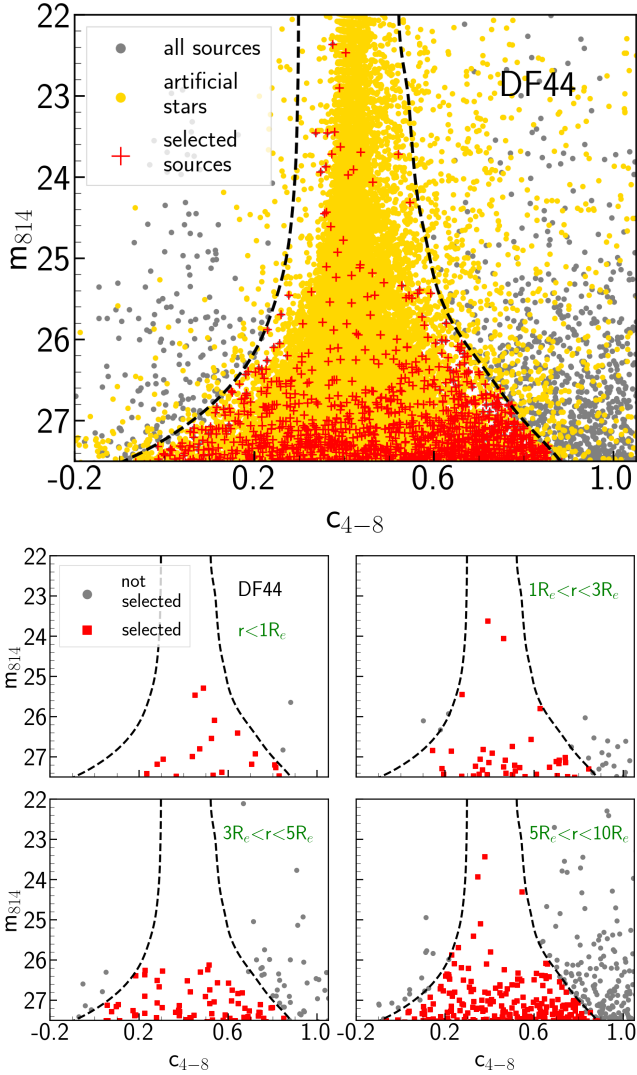


Figure 4. Top: Compactness index (c_{4-8}) - magnitude diagram for DF44 in its primary frames ($F814W$). The boundaries of point source selection are indicated with black dashed curves. All the sources in the primary frames, simulated stars and selected point sources are shown in grey dots, yellow dots and red crosses respectively. Bottom: Similar diagram as the diagram on top for sources in different radial distances from the host UDG. Selected sources and not-selected (discarded) sources are shown in red and grey dots.

Because the secondary data are shallower than the primary, completeness will be a function of colour. To account for this, we repeat the artificial star simulations for the secondary filter and measure its completeness. To derive the combined completeness, we assume that GCs have average colours of $m_{606} - m_{814} = 0.35$ mag and $m_{475} - m_{814} = 0.80$ mag (based on the photometric prediction of the E-MILES stellar library for a 10-14 Gyr single stellar population with metallicities between $-2 < Z < 0.5$; (Vazdekis et al. 2010, 2016)). The combined completeness function is shown in Fig. 5 in purple. The multi-wavelength catalogues are 75 per cent complete around the expected GCLF turn-over, around $m_{814} \sim 27.0$ mag (Miller & Lotz 2007; Kundu & Whitmore 2001).

We apply colour cuts to the selected point sources. We use the colour $0.1 < m_{606} - m_{814} < 0.75$ mag for DFX1 and $0.4 < m_{475} - m_{814} < 1.5$ mag for rest of the sample. This colour range is estimated

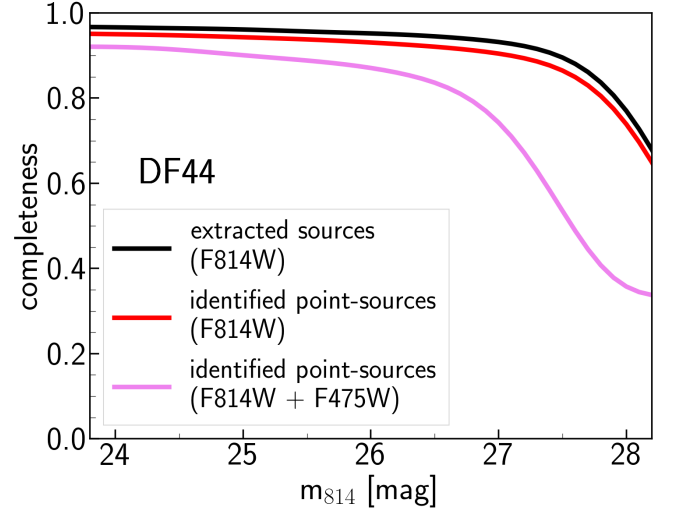


Figure 5. The completeness of source extraction (black), point source selection (red for $F814W$ primary filter) and source selection after including the secondary filter (shallower data, purple), for the galaxy DF44.

based on the photometric prediction of the E-MILES stellar library as described earlier. We retain candidates that exceed these limits by less than 1σ .

In Fig. 6 we demonstrate the effects of cross-matching and colour-selection in removing sources in the DF44 field (for the other UDGs in Fig. A7) for candidates within $3R_e$ of their host galaxies. We highlight in grey the (suspected) cosmic rays that are not cleaned by L.A.Cosmic but are removed after cross-matching between primary and secondary images. The red triangles highlight those sources rejected due to their colour. In Fig. 7 we show the GC candidates in DF44 before and after applying the colour-cuts (left and right panels).

As already mentioned, even the best set of criteria cannot exclude the possibility of contamination. As such, the surviving objects are only GC candidates. To correct for contamination, we estimate and take into account the average properties of objects that satisfy all of our criteria but lie sufficiently far from the UDG that they are unlikely to be associated with the UDG. These contaminants may include surviving cosmic rays, Galactic stars, or actual GCs, perhaps free-floating Coma GCs, that are not associated with the targeted UDG. In Fig. 8 we show the selected GC candidates after compactness and colour selection for the six UDGs in our sample. We provide a wider view in Fig. 9.

4 RESULTS

We now use our GC candidate catalogues to explore the GC luminosity function, radial profile, total number, and colours.

4.1 GC Luminosity Function

The GCLF describes the number of GCs as a function of luminosity. Observations of GCs in other classes of galaxies show that this function, when expressed in terms of the GC magnitude, can be approximated by a Gaussian function (Secker & Harris 1993) described by the value of the mean, or turn-over, magnitude (μ_{peak}) and its width (σ). These parameters carry information on the formation history and dynamical evolution of GCs in galaxies, in this

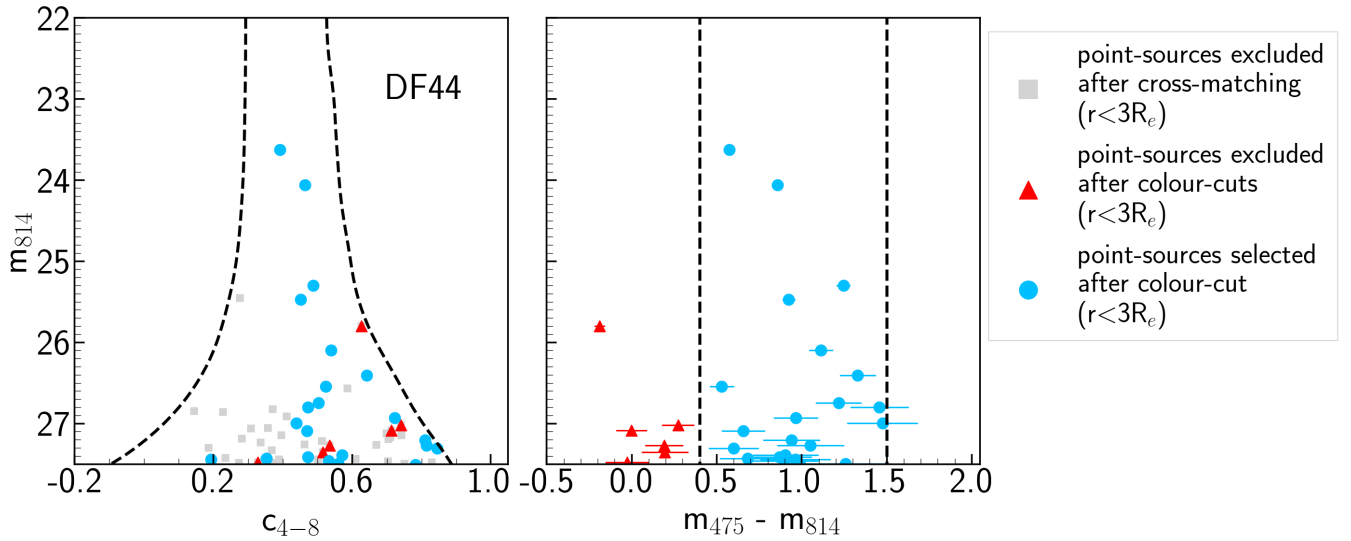


Figure 6. Compactness index (c_{4-8}) - magnitude diagram (left) and colour-magnitude diagram (right) of point sources within $3R_e$ of DF44. After cross-matching sources in the primary data with the extracted sources in the secondary data, those without corresponding detection are likely remaining cosmic rays and rejected (grey symbols). With the colour limits as indicated in the right panel (vertical dashed lines), the remaining sources are either selected (blue) or rejected (red) as GC candidates.

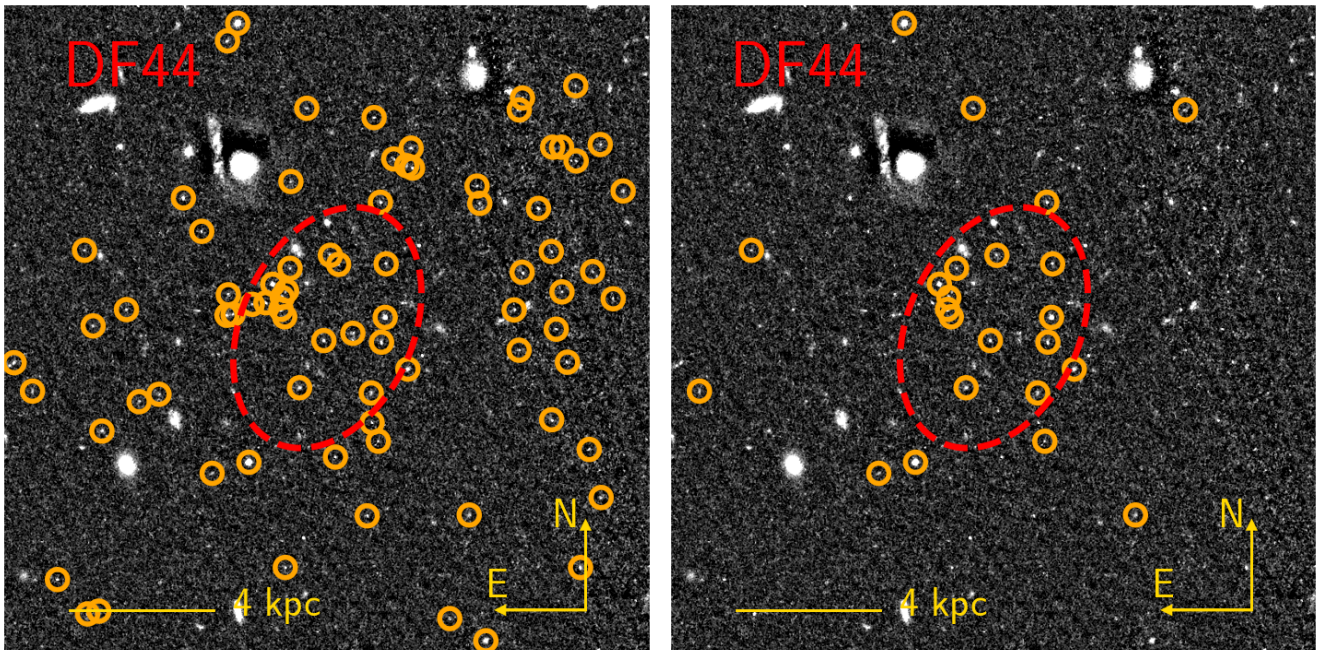


Figure 7. Selected point sources (left panel) and remaining sources after cross-matching and colour selection (right panel) for DF44. Sources brighter than $F_{814W} = 27.5$ mag are shown. The dashed red ellipse corresponds to the effective radius of the galaxy.

case for large UDGs. One puzzling aspect of GC populations is the near universality of the peak of the GCLF (Rejkuba 2012). Over the range of environments in which GCs are found one might expect both different formation conditions and significantly different rates of tidal disruption and dissolution.

Our large UDGs are expected to host a few tens of GCs each of which about half of that many are brighter than the GCLF turn-over magnitude (Peng & Lim 2016; Beasley & Trujillo 2016; Saifollahi et al. 2021). Additionally, we are 75 per cent complete near the peak

of the GCLF, and so expect a fraction (more than 75 per cent) of that half in our catalogues. Such low numbers render the resulting GCLFs and their parameters (μ_{peak} and σ) highly uncertain for individual galaxies. Instead, we construct the combined GCLF and adopt its parameters for all our galaxies. To do this, we select GC candidates around each galaxy within an ellipse with a semi-major axis of $1.5R_e$ and the axis ratio and position angle of the host UDG. The value of $1.5R_e$ for the semi-major axis is a compromise between encompassing the entire GC system and minimizing contamination. The choice

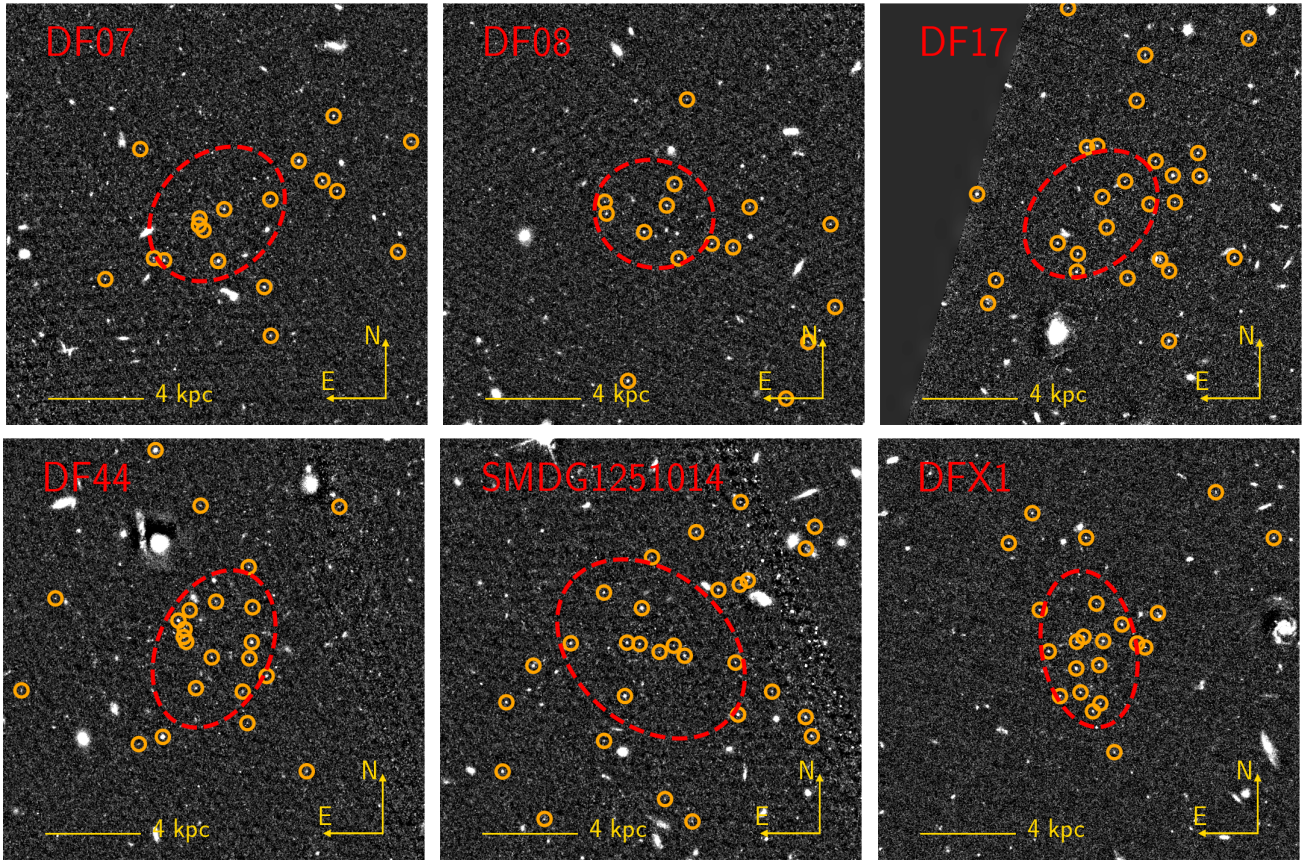


Figure 8. GC candidates selected based on compactness index and colours. Sources brighter than $F814W = 27.5$ mag are shown (for DFX1, brighter than $F606W = 28.0$ mag).

of axis ratio and position angle is supported by the expectation that (in-situ) GCs follow the azimuthal distribution of the field stars in galaxies (Kissler-Patig et al. 1997; Kavelaars 1998; Gómez et al. 2001) and we will return to this choice later (Section 4.2).

To correct statistically for remaining contamination, we estimate a combined background using selected GC candidates farther than $5R_e$ from each galaxy. We normalize by the area and subtract from our observed LF within $1.5R_e$. We then correct for incompleteness (source extraction in both bands and point source selection) to obtain our final estimate of the GCLF. In Fig. 10 we present this combined GCLF for the six UDGs in our sample and the Gaussian fit. We find for $F814W$ that $\mu_{\text{peak},814} = -8.14 \pm 0.14$ mag and $\sigma_{814} = 0.79 \pm 0.06$ mag, which corresponds to $\mu_{\text{peak},I,AB} = -8.10 \pm 0.14$ mag⁶.

Within the uncertainties, the turnover we measure is the same as that observed for dwarf ellipticals ($\mu_{I,AB} = -8.1$; Miller & Lotz 2007) and less than 3σ different from that found for more massive ellipticals ($\mu_{\text{peak},I,AB} = -8.46$; Kundu & Whitmore 2001). Similarly, our measured value of $\sigma_{814} = -0.79 \pm 0.06$ is consistent with the typical value measured for dwarf elliptical galaxies ($\sigma < 1$ mag; Miller & Lotz (2007); Harris et al. (2014)). In turn, this is different from what found in more massive galaxies ($\sigma > 1.2$ mag; Harris et al. (2014)).

The stacked GCLF described here is representative of the GCs around UDGs with large effective radii. Because the completeness-corrected estimates of the total number of GCs in each galaxy, N_{GC} ,

that we present later (in Section 4.3) are sensitive to the turn-over magnitude, we now search for possible galaxy-to-galaxy variations by repeating the above exercise for each individual UDG, but adopting σ from the composite GCLF. In Fig. 11 we present the individual galaxy GCLFs and the estimated turn-over magnitude. We find no evidence for significant ($> 2\sigma$) variations in $\mu_{\text{peak},814}$.

4.2 GC Distribution

Given the relatively small number of GCs per UDG, it is understandable that there have been only a few studies of the GC distribution in UDGs. One way to describe the radial distribution is with the GC half-number radius, R_{GC} , which is the radius containing half of all of the GCs in that particular system. Peng & Lim (2016) estimated $R_{\text{GC}} = 1.5 R_e$ for DF17, which was later adopted in several studies to help determine the completeness corrections needed to estimate N_{GC} (van Dokkum et al. 2017; Lim et al. 2018). Amorisco et al. (2018) found that, even in UDGs with abundant GC systems, $R_{\text{GC}}/R_e < 2$ with high probability, with several systems better described by $R_{\text{GC}}/R_e \lesssim 1$. More recent estimates of R_{GC} for DF44⁷ (Saifollahi et al. 2021), for MATLAS-2019 (Müller et al. 2021) and for NGC1052-DF2 (Montes et al. 2021) find $R_{\text{GC}} \leq R_e$.

⁷ van Dokkum et al. (2017) also estimated R_{GC} from a stacked GC distribution for DF44 and DFX1 and found $R_{\text{GC}} = 2.2^{+1.3}_{-0.7} R_e$, however given the large uncertainties in their estimation, they adopted the R_{GC} value from Peng & Lim (2016).

⁶ using $m_{F814W,AB} = m_{I,AB} - 0.04$ mag (Gennaro, M., et al. 2018)

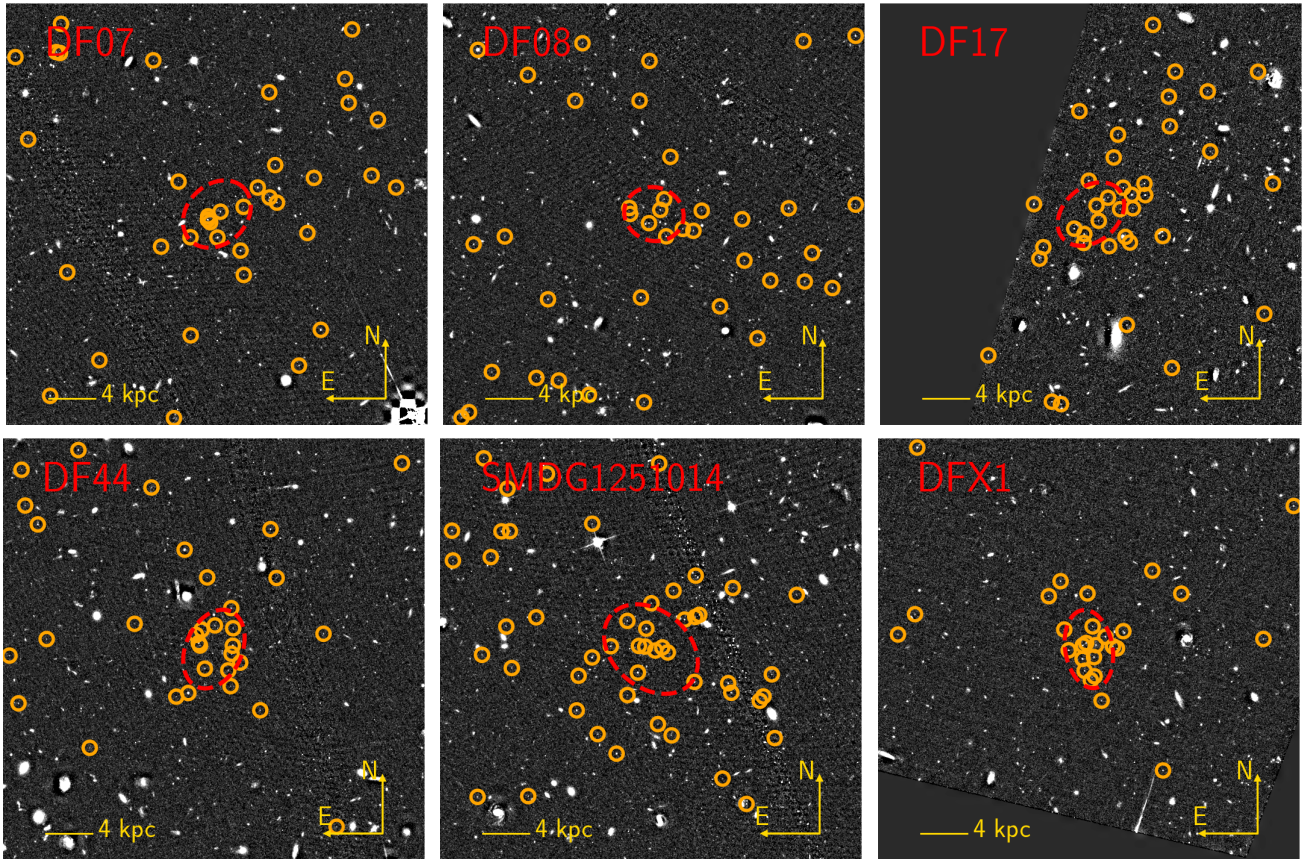


Figure 9. Zoomed-out view of GC candidates selected based on compactness index and colours. Sources brighter than $F814W = 27.5$ mag are shown (for DFX1, sources brighter than $F606W = 28.0$ mag are shown).

Again, due to statistical uncertainties, we opt first to work with the composite sample. Here, we describe the radial profile of the combined GC sample using a Sérsic model and measure both the GC half number radius R_{GC} and the Sérsic index n . To combine the candidates from the different galaxies, we normalize the radial distances relative to the corresponding host effective radius. We select only the GC candidates within $R_{GC}/R_e = 3$. We doubled the radial distance cut from that used earlier to have better leverage on the model fitting.

To obtain the parameters, we apply a maximum likelihood estimator (MLE), as in Saifollahi et al. (2021). The MLE approach uses a large number of simulations (here 1,000) and in each run, it accounts for the background contamination by randomly excluding a number of GCs corresponding to the number of expected background sources from the background luminosity function. In Fig. 12 and Table 3 we present the derived Sérsic parameters and radial profile of the combined GC sample. We find $R_{GC}/R_e = 1.09^{+0.13}_{-0.14}$ and $n = 0.68^{+0.30}_{-0.19}$. This value of R_{GC} is consistent with that found for local dwarf galaxies in groups and in the Virgo cluster ($R_{GC} = 1.06^{+0.21}_{-0.18} R_e$ and $R_{GC} = 1.25^{+0.24}_{-0.18} R_e$, respectively), as well as for galaxies from that sample selected to span the same stellar mass range ($7.8 < \log(M_*/M_\odot) < 8.4$; $R_{GC} = 1.40 \pm 0.38 R_e$; Carlsten et al. 2021). In Fig. 14 we compare the individual R_{GC}/R_e values with a set of UDG properties and find no significant trends.

We also estimate R_{GC} for each UDG. For DF17, we find $R_{GC} = 1.54^{+0.28}_{-0.30} R_e$, consistent with the value from Peng & Lim (2016). For DF44, using a new dataset, we measure

$R_{GC} = 0.78^{+0.44}_{-0.30} R_e$, consistent with the reported value in Saifollahi et al. (2021) ($R_{GC} = 0.8^{+0.3}_{-0.2} R_e$).

In Fig. 13 we inspect the azimuthal distribution of the composite GC candidate sample out to $1.5 R_e$ relative to the distribution of stellar light. Measuring the azimuthal distribution relative to the position of the stellar major axis, the GC numbers clearly peak around 0° and 180° , confirming the alignment of the two distributions that we had assumed in §4.1.

4.3 GC Number

The number of GCs in a galaxy (N_{GC}) is known to scale more strongly with the total mass of the host galaxy (M_{total}) (Harris et al. 2013) than with the stellar mass. This somewhat surprising result can be recovered for massive galaxies with the total masses typically larger than $10^{11} M_\odot$, at least, as the natural outcome of hierarchical formation (Boylan-Kolchin 2017; El-Badry et al. 2019; Valenzuela et al. 2021). Recent simulations incorporating GC formation in cosmological hydrodynamical simulations (E-MOSAICS, Kruijssen et al. 2019; Pfeffer et al. 2018) also reproduce the sense of the relation between N_{GC} and M_{total} (Bastian et al. 2020) for galaxies more massive than $5 \times 10^{11} M_\odot$. These total masses are similar or slightly larger than the total mass of UDGs in our sample. However, among lower-mass galaxies, where the stellar mass is observed to drop precipitously, there is no corresponding observed drop in N_{GC} and the origin of this relation remains in question (Forbes et al. 2018). As such, more measurements of N_{GC} in low stellar mass systems are needed to

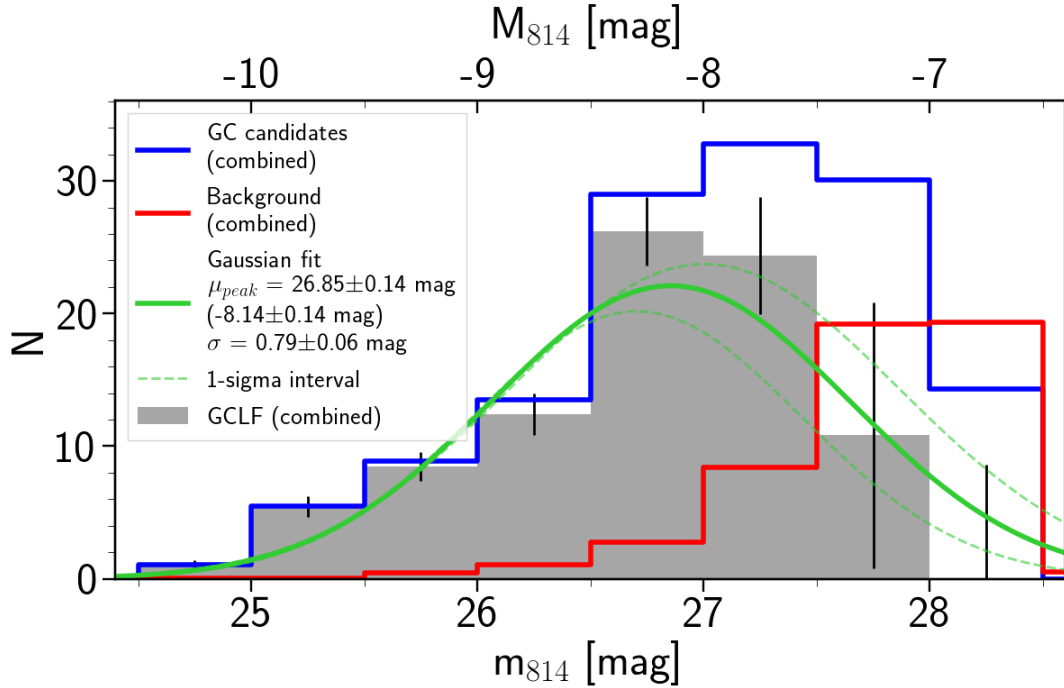


Figure 10. The combined globular clusters luminosity function (GCLF) in $F814W$ (grey histogram), the best-fit Gaussian function (green curve), the combined GCLF before background subtraction (blue histogram) and the background luminosity function (red histogram). The errorbar at a given magnitude bin is the sum of uncertainties (Poisson noise) in background subtraction and incompleteness correction in that bin.

confirm the trend and explore possible physical sources of scatter. The relation between N_{GC} and M_{total} has been assumed to hold for UDGs, although that is worth confirming, and has been utilized as an alternative to direct, but more observationally expensive, ways to estimate masses. We will also estimate the total masses using N_{GC} .

We measure N_{GC} as follows. First, we select the GC candidates within $3R_{GC}$ of each galaxy. We estimate that within this radius, for the mean Sérsic index $n = 0.68$ that describes the radial distribution of GCs in our UDGs, we capture more than 95 per cent of all the GCs (Trujillo et al. 2001). Then, because our data does not cover the full GCLF magnitude range, we assume that the GCLF is symmetric around μ_{peak} and correct the measured N_{GC} up to μ_{peak} for fainter GCs by doubling the number. We make two different estimates of N_{GC} . In the first, which we indicate with N_{GC} , we use our estimate of R_{GC}/R_e for each individual galaxy, and in the other, which we refer to with N_{GC}^* , we use the mean value of R_{GC}/R_e estimated from the composite. We find no difference between these two approaches within the uncertainties (Fig. 15). Therefore, we adopt our values N_{GC} in the following. In Table 3 we present the final values of R_{GC}/R_e , n and N_{GC} for each galaxy. The uncertainties in N_{GC} take into account the uncertainties in R_{GC} , μ_{peak} and the background number density.

Adopting the N_{GC} - M_{total} relation, $M_{total} = 5.12 \times 10^9 \times N_{GC} M_{\odot}$ (drawn from Harris et al. 2017 relation between total GC population mass and halo mass, and adopting an average GC mass of $2 \times 10^5 M_{\odot}$), we find total masses for our UDGs between $0.51^{+0.26}_{-0.41} \times 10^{11}$ and $1.54^{+0.26}_{-0.20} \times 10^{11} M_{\odot}$ and a corresponding range of total to stellar mass ratios between 300 to 1,000.

In Fig. 16 we show the relations between N_{GC} and other UDG properties. As expected, the number of GCs increases with the luminosity of the galaxy, as a proxy for its stellar mass. The same increasing trend is observed between N_{GC} and other galaxy param-

eters, which can be the outcome of the existing scaling relations between the properties of UDG (such as that between R_e and total mass (Zaritsky 2017).

When the UDG N_{GC} values are compared to those of other galaxies, the UDGs show systematically twice larger N_{GC} at a given stellar mass (Fig. 17). The galaxy sample in Fig. 17 includes galaxies in the Virgo cluster (Peng et al. 2008; Carlsten et al. 2021), the Fornax cluster (ACSFCS, Liu et al. 2019) and galaxy groups in the local volume (Carlsten et al. 2021). Our UDGs are in the Coma cluster, which is more massive than the other two clusters, and the relative increase in N_{GC} at a given stellar mass may be an indication of environmental effects in GC formation or UDG evolution (Peng et al. 2008; Carleton et al. 2021; Carlsten et al. 2021). It is noteworthy that among the best-studied UDGs in term of their GCs, the UDG known as MATLAS-2019 (Habas et al. 2020) with $R_e = 2.2$ kpc (smaller effective radius than our UDGs) shows a large number of GCs for its stellar mass (Müller et al. 2021; Danieli et al. 2021). Although it constitutes a single example, it lies in a low-density environment and is therefore a counterexample to the possible trend with environment.

In the middle panel of Fig. 18 we show a statistically significant positive correlation between R_{GC} and N_{GC} for the six UDGs in our sample (coloured points), suggesting that more massive haloes (with more GCs) have larger R_{GC} . The trend is still there, but with less statistical significance after normalizing R_{GC} by R_e , suggesting that some of the effect in the top panel is driven simply by the overall size of the system. Nevertheless, some indication remains that even after accounting for the differences in R_e , the distribution of globular clusters is more extended in the more massive galaxies. Furthermore, Fig. 18 compares these UDGs to a sample of dwarf galaxies in the

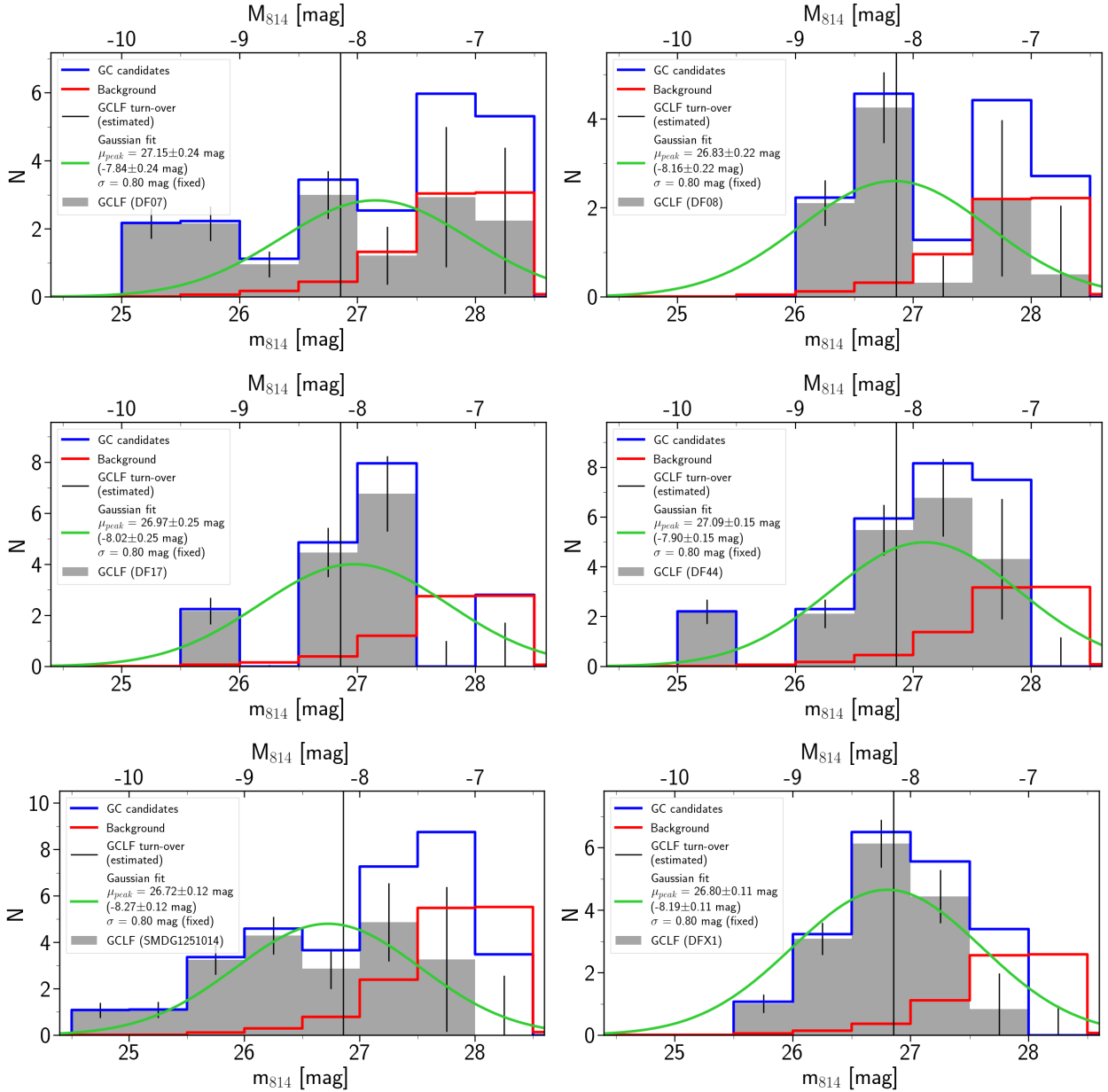


Figure 11. As Fig. 10, but now showing the GCLF in F814W for individual UDGs and the best-fit Gaussian function with a fixed $\sigma = 0.80$ mag.

Virgo cluster (Carlsten et al. 2021⁸). We exclude SMDG1251014 and DF17 from this comparison because the dwarf sample does not provide enough points for their total mass (based on N_{GC}). The four remaining UDGs (DF07, DF08, DF44 and DFX1) have R_e on average 3 times larger than the average value for dwarfs of the same (total) mass while their R_{GC} is only 1.5 times higher which leads to a lower R_{GC}/R_e for these UDGs. The implications of this result are discussed in Section 5.

⁸ The sample that we used here consists of those 18 dwarf galaxies for which R_{GC} has been estimated by the authors. Therefore this sample does not include all of the Virgo cluster dwarf galaxies in Carlsten et al. (2021), but the ones with enough GCs that R_{GC} could be estimated.

4.4 GC Colour

GCs around massive galaxies show complex colour distributions that are mostly attributed to metallicity differences (Brodie & Strader 2006). It is hypothesized that massive galaxies host both in-situ metal-rich/red GCs and ex-situ metal-poor/blue GCs. The latter formed in lower-mass galaxies, where the bluer colour is attributed to lower metallicity and accreted GCs. One of the implications of this scenario is a correlation between GC average colour and galaxy luminosity (Peng et al. 2006). Finally, the GC colour distributions and a comparison to the properties of the UDG main body may provide clues on star/GC formation episodes within UDGs.

We measure the GC average colour ($m_{475} - m_{814}$) and colour spread ($\sigma_{m_{475} - m_{814}}$) using GCs within $1.5 R_e$ (Table 3) and compare those quantities to the UDG properties in Fig. 19. The average GC colours cover a range between 0.78 mag and 1.13 mag with an

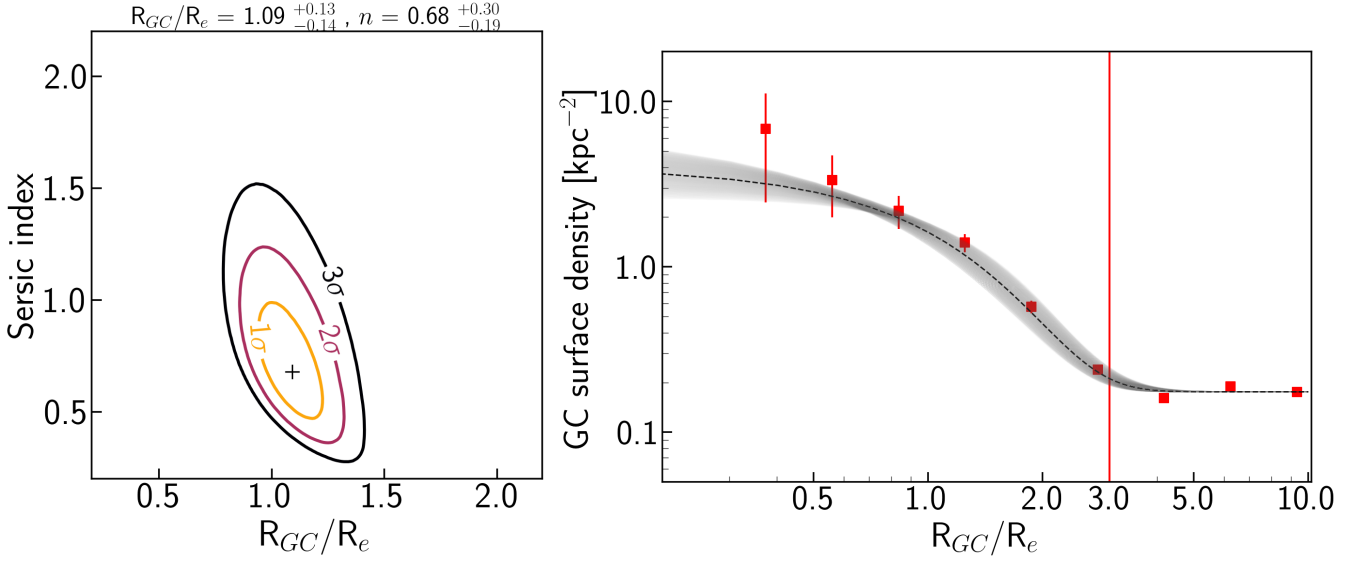


Figure 12. Left: Likelihood maps for the derived Sérsic parameters of the combined GC distribution. Right: The combined GC radial profile and the derived Sérsic profile from MLE. The estimated profile (black dashed line) is not a fit to the binned data. The grey region indicates the 1σ uncertainties in the estimated Sérsic profile (based on our maximum likelihood estimator). The red vertical line indicates $R_{GC} = 3R_e$, which is the radius-cut that is used for selecting GCs for estimating their Sérsic parameters.

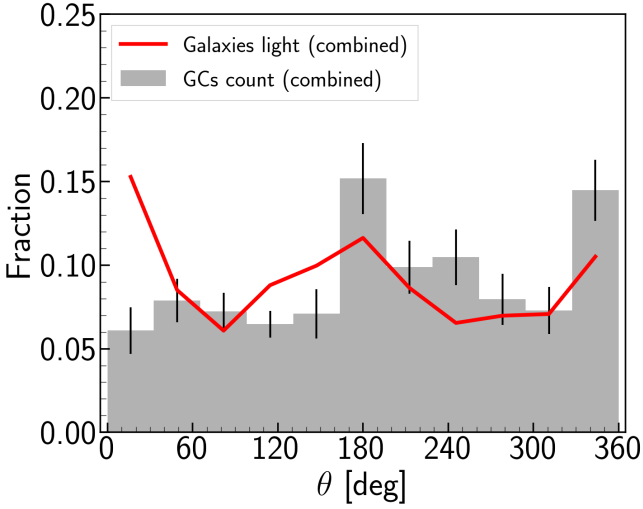


Figure 13. The stacked azimuthal distribution of the globular clusters (grey) and galaxies field stars (red) relative to the galaxy's major axis. The peak in GC number around $0/360^\circ$ and 180° corresponds closely to a peak in the galaxies light. GCs are thus well aligned with the stars.

average value of 0.95 mag. This value is consistent with the average colour of GCs around lower luminosity galaxies (Peng et al. 2006). As evident from Fig. 19, these colours do not show any evident correlation with UDG properties. Furthermore, in one panel of this figure (second panel from right) we compare GC colour to galaxy host colour (top, second plot from right), where the diagonal line separates the UDGs with redder and bluer GC population than their corresponding field stars. We do not see any obvious pattern and some are slightly redder than their host UDG while some are slightly bluer. GC colour spreads range between 0.1 mag to 0.3 mag and increase for the brighter UDGs.

5 DISCUSSION

We aim to answer three questions regarding these large effective radius UDGs :

- (i) Do UDGs with L^* -like haloes exist?
- (ii) Are GCs in UDGs similar to those in other galaxies?
- (iii) Can GC properties constrain UDG formation models?

5.1 Do UDGs with L^* -like haloes exist?

The first studies on UDGs speculated that UDGs might be hosted by L^* -like (e.g. like that of the Milky Way) dark matter halos of mass $\sim 10^{12} M_\odot$ (van Dokkum et al. 2015a; Koda et al. 2015; Yozin & Bekki 2015; van Dokkum et al. 2016, 2017). This idea has lost appeal as dynamical mass measurements demonstrated that the most massive UDGs have masses of at most a few $\times 10^{11} M_\odot$ (Beasley et al. 2016; Toloba et al. 2018; Amorisco et al. 2018; van Dokkum et al. 2019), placing them among massive dwarf galaxies like the LMC.

Among known UDGs, DF44 is an exceptional case and the original one thought to possibly have an L^* -like halo, in part because the initial estimates found $N_{GC} = 94^{+25}_{-20}$ (van Dokkum et al. 2016) and $N_{GC} = 74 \pm 18$ (van Dokkum et al. 2017). Subsequent kinematic mass estimates based on spatially resolved kinematics ($M_{\text{halo}} = 1.6^{+5.0}_{-1.2} \times 10^{11} M_\odot$; van Dokkum et al. 2019), N_{GC} measurements ($N_{GC} = 21^{+7}_{-9}$; Saifollahi et al. 2021) and constraints from X-ray data (Bogdán 2020) have helped push the mass estimates downward. We now extend the N_{GC} measurements to an additional 5 UDGs with properties similar to those of DF44 and confirm that these are consistent with being in halos of $\sim 10^{11} M_\odot$ rather than $\sim 10^{12} M_\odot$. In agreement with the recent consensus, we conclude that we do not find evidence for physically large UDGs inhabiting L^* -like halos.

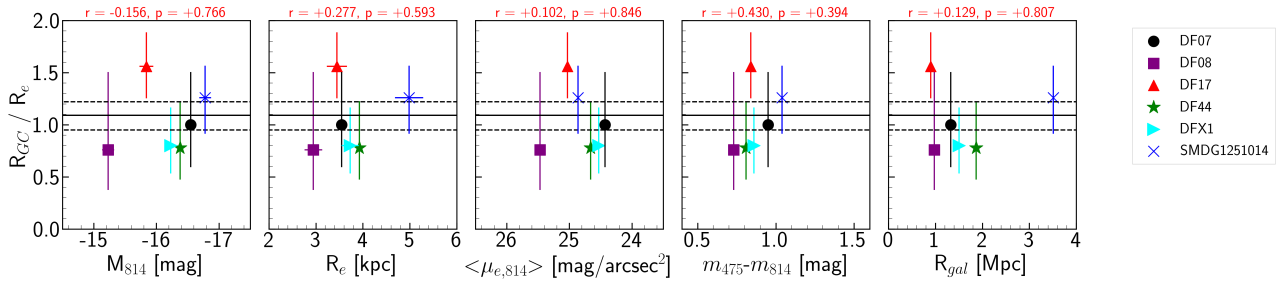


Figure 14. The ratio between the GC half number radius R_{GC} and galaxy effective radius R_e for the UDG sample. The horizontal lines indicated the estimated value from combined GC distribution and its standard deviation. The R_{GC}/R_e values do not show any strong correlation with UDG properties: (from left to right) absolute magnitude in $F814W$, effective radius, effective surface brightness in $F814W$, colour and clustercentric distance).

Table 3. The derived properties of the GCs around the UDGs in the sample. Columns from left to right represent galaxy name (a), the ratio between GC half-number radius and galaxy’s half light radius (b), the Sérsic index of the GC radial profile (c), GC number count (d), average colour and colour spread of GCs (e, f) and the derived total mass using N_{GC} (g). For DFX1, the average colour is converted from $m_{606} - m_{814}$ to $m_{475} - m_{814}$ using transformations in Blakeslee et al. (2010).

Galaxy	R_{GC}/R_e	n	N_{GC}	$\langle m_{475} - m_{814} \rangle$	$\sigma_{\langle m_{475} - m_{814} \rangle}$	M_{total}
(a)	(b)	(c)	(d)	(e)	(f)	(g)
DF07	$0.98^{+0.50}_{-0.38}$	$1.12^{+1.86}_{-0.88}$	22^{+5}_{-7}	0.78 ± 0.05	0.16	$1.12^{+0.26}_{-0.36} \times 10^{11}$
DF08	$0.68^{+0.52}_{-0.38}$	$0.36^{+3.50}_{-0.16}$	10^{+5}_{-8}	0.94 ± 0.05	0.14	$0.51^{+0.26}_{-0.41} \times 10^{11}$
DF17	$1.54^{+0.28}_{-0.30}$	$0.20^{+0.34}_{-0.00}$	26^{+17}_{-7}	1.13 ± 0.05	0.15	$1.33^{+0.87}_{-0.36} \times 10^{11}$
DF44	$0.78^{+0.44}_{-0.30}$	$0.94^{+1.74}_{-0.54}$	20^{+6}_{-5}	1.07 ± 0.08	0.28	$1.02^{+0.31}_{-0.26} \times 10^{11}$
SMDG1251014	$1.28^{+0.32}_{-0.32}$	$0.38^{+0.72}_{-0.18}$	30^{+5}_{-4}	0.93 ± 0.06	0.25	$1.54^{+0.26}_{-0.20} \times 10^{11}$
DFX1	$0.8^{+0.34}_{-0.26}$	$1.06^{+1.20}_{-0.54}$	17^{+5}_{-6}	0.86 ± 0.06	0.22	$0.87^{+0.26}_{-0.41} \times 10^{11}$

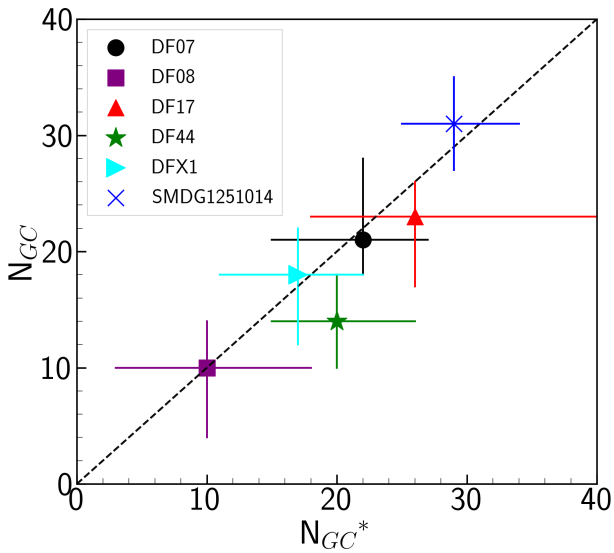


Figure 15. Comparison between the number of GCs derived using individual R_{GC}/R_e values (N_{GC}) and combined R_{GC}/R_e value (N_{GC}^*). The dashed line indicates the one-to-one values of N_{GC} and N_{GC}^* .

5.2 Are GCs in UDGs similar to those in other galaxies?

We find that the GC numbers, the GCLF (μ_{peak} and width σ), GC radial distribution, and GC average colour in our UDGs are consistent with the values derived for GCs in dwarf galaxies. Among these, N_{GC} has received the most attention because some studies claim that UDGs host more GCs than other galaxies of the same stellar mass (van Dokkum et al. 2017; Lim et al. 2018, 2020, but see also Amorisco et al. 2018; Prole et al. 2018). Given the heterogeneity of the UDG population, all the previous conclusions can be correct.

We have focused on UDGs with large R_e . These are thought to be the most massive (Zaritsky 2017) and have, at least in a couple of cases, been shown to host significant numbers of GCs. With a sample of six such UDGs, we can investigate whether any differences are systematic among UDGs or susceptible to object-to-object variation. Our images are deeper than the above-mentioned work, which allows us to achieve lower measurement uncertainties. As we show in Fig. 17, these UDGs are at the upper end of the N_{GC} range for galaxies of the same stellar mass. We find that N_{GC} for these UDGs is roughly twice that of the average value for galaxies of the same stellar mass. Nonetheless, they are well within the global distribution considering the scatter of the relation. As noted by Carleton et al. (2021), whose model attributes such an offset not to an overabundance of GCs but rather to a paucity of stars in UDGs, there are different ways to view the result. Because we do not have independent measurements of M_{total} for the full sample, we cannot yet determine if these systems

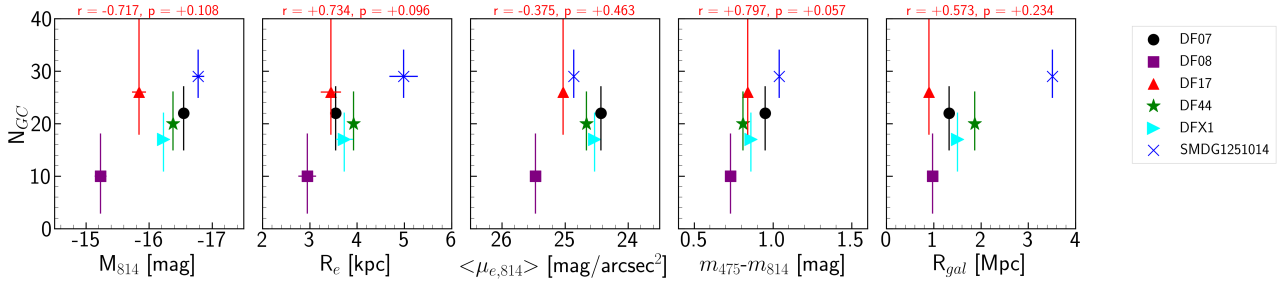


Figure 16. N_{GC} versus galaxy property for our UDG sample (from left to right: absolute magnitude in $F814W$, effective radius, effective surface brightness in $F814W$, colour and clustercentric distance). The Pearson correlation coefficient, r , and p -values are included above each panel.

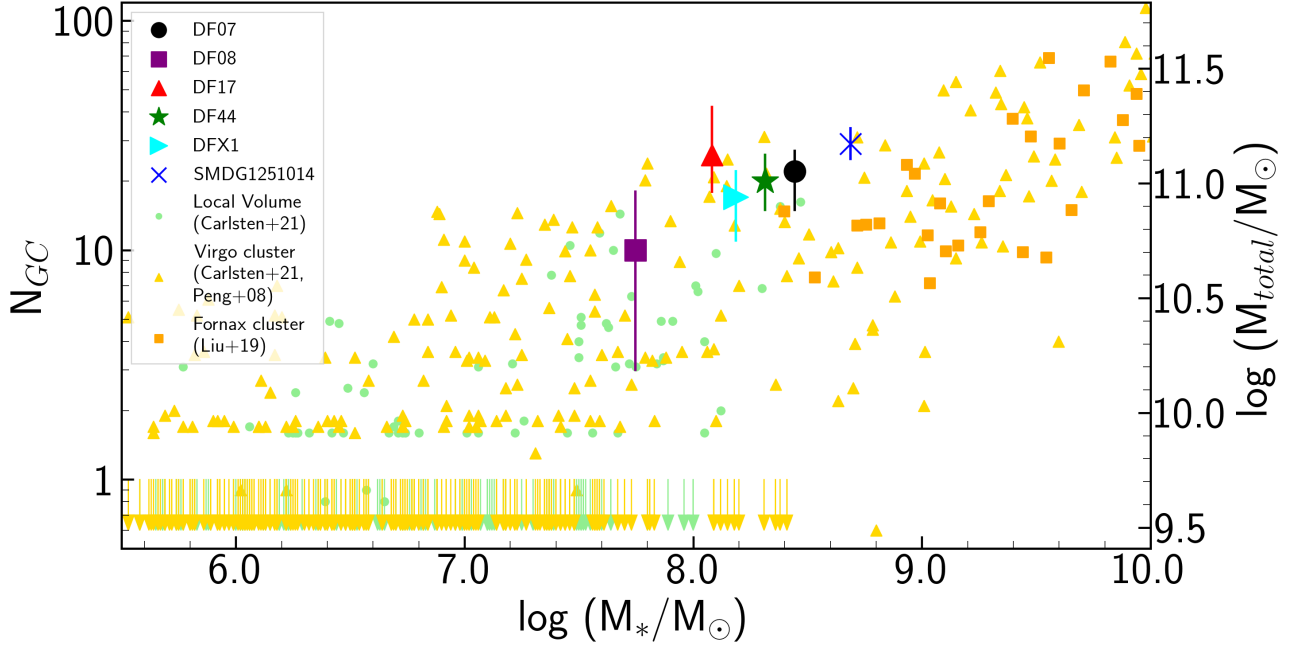


Figure 17. N_{GC} versus the stellar mass, M_* , for our UDGs and for galaxies in the Virgo cluster (yellow triangles), Fornax cluster (orange squares) and galaxy groups in the local universe (green dots). Galaxies where N_{GC} is consistent with zero are shown with the downward arrows. On the right side of the diagram we present the corresponding total galaxy mass calculated using $M_{total} = 5.12 \times 10^9 \times N_{GC} M_{\odot}$. Most galaxies from the literature with masses $\log(M_*/M_{\odot}) < 8.5$ are dwarf early type galaxies and only five are considered to be UDGs. Stellar masses for the UDGs are calculated based on equations provided in [Into & Portinari 2013](#). The Pearson correlation coefficient, r , and p -values are included above each panel.

are overabundant in GCs or deficient in stars. Indications from DF44 suggest the latter.

5.3 Can GC properties constrain UDG formation models?

Several UDG formation models are proposed to explain the current appearance of these galaxies. These models commonly describe UDGs as dwarf galaxies that undergo various processes that shape the current properties of UDGs. Until now, all the proposed models agree that cluster UDGs are quenched due to environmental effects taking place in galaxy groups and galaxy clusters. These models provide different explanations for the low surface brightness and large effective radius. The properties of GCs, as studied here, provide another set of observables to constrain the proposed models.

The elevated N_{GC}/M_* of UDGs argues against models that seek to explain the low surface brightness nature of UDGs primarily by redistributing the stars to larger radii ("high-spin", "tidal interaction",

"stellar feedback" models⁹). [Villaume et al. \(2022\)](#) made a similar conclusion based on the stellar population parameters of DF44. These results are independent of the total mass of the galaxy.

To the degree that such models also affect the star formation efficiency, for example, the "high-spin" model also presumably leads to lower gas densities and lower star formation rates, the models may be salvageable. The N_{GC} values suggest that unless a model specifically predicts a greater GC formation efficiency, then it must account for a lower than average star formation efficiency. However, such modifications to the mean star formation efficiency must occur without affecting the GC formation efficiency. This suggests that whatever is responsible acts after the bulk of GC formation. Additionally, the astrophysical processes involved in these models (i.e. dynamical heating in the "tidal interaction" model) have a similar impact on the distribution of stars and GCs. In this case, it is expected that the

⁹ Here and in Table 4, the "stellar feedback" model only refers to the model proposed in [Di Cintio et al. \(2017\)](#).

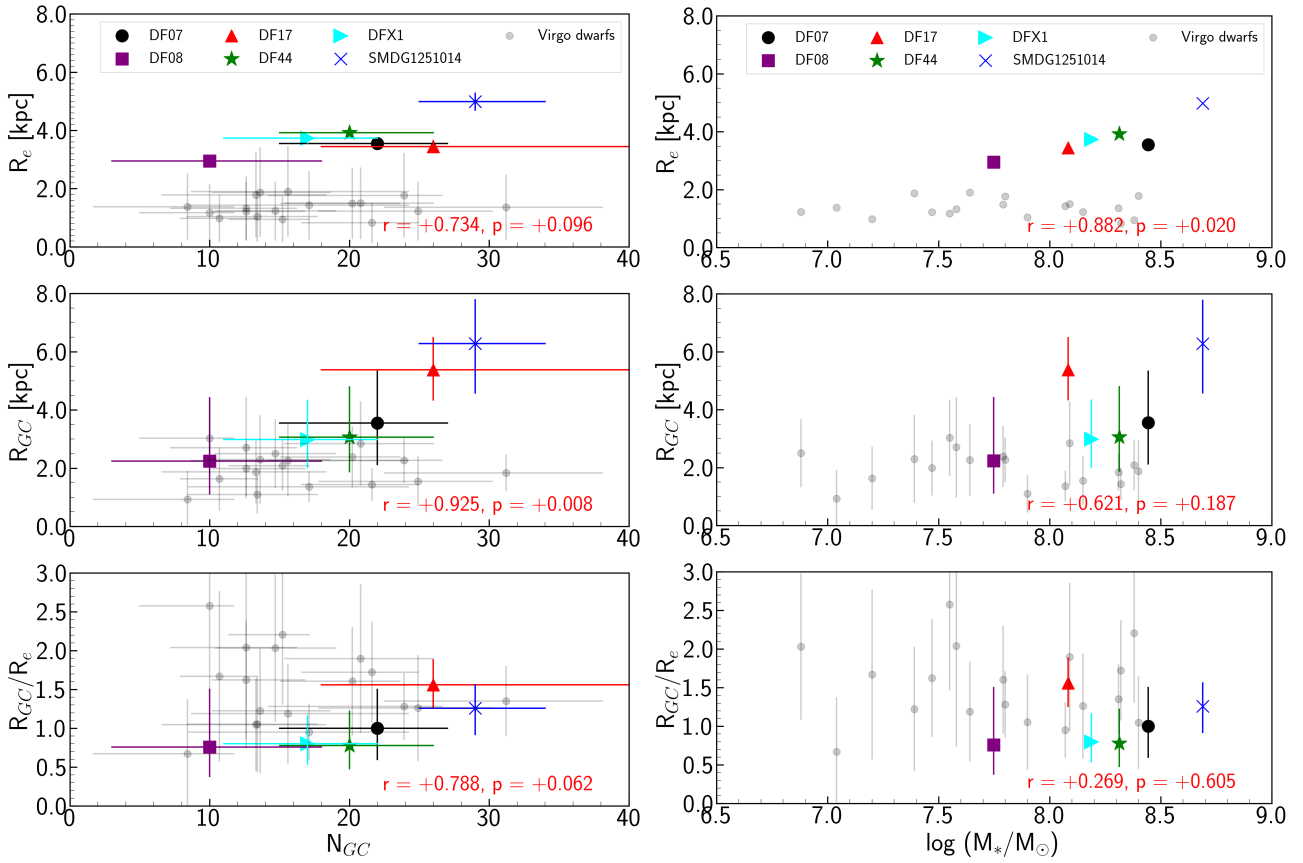


Figure 18. The galaxies effective radius (R_e , upper frames), GC half-number radius (R_{GC} , middle frames) and their ratio (R_{GC}/R_e , lower panel) as a function of the GC total number (left) and the host galaxy stellar mass (right) for the UDGs in this work and the dwarf sample (Carlsten et al. 2021). The Pearson correlation coefficient, r , and p -values are included within each panel.

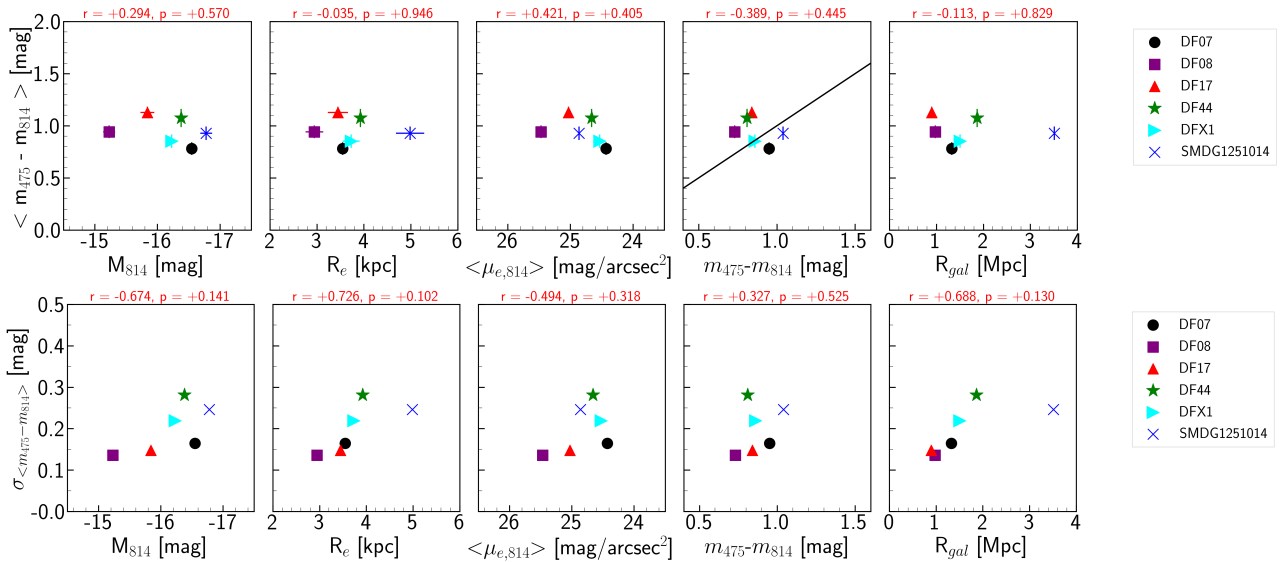


Figure 19. GC average colour and colour spread versus the properties of host UDGs: (from left to right) absolute magnitude in $F814W$, effective radius, effective surface brightness in $F814W$, colour and clustercentric distance. For DFX1, the values are converted from $m_{606} - m_{814}$ to $m_{475} - m_{814}$ using the transformations in Blakeslee et al. (2010). Galaxies below/above the diagonal line (second diagram from right) have bluer/redder GCs than their field stars. The Pearson correlation coefficient (r) and p -values are indicated on top of the diagram.

Table 4. The implications of the observed GC properties for the proposed formation models. Here we discuss implications of two observed GC properties for the UDG formation models in the literature: i. the excessive GC number of UDGs compared to dwarf galaxies, ii. the similarity between the radial profile of GCs and the fields stars of UDGs (R_{GC}/R_e) (✓: observable favours this model, ✗: observable disfavors this model).

Observable	Failed dwarf galaxy	Tidal interactions	Stellar feedback	High-spin dwarfs	Lack of mergers
i. Excessive GC number	✓	✗	✗	✗	✓
ii. GC radial profile	✓	✗	✗	✗	✓

star and the GC distribution within galaxies expand (R_e and R_{GC} increase) similarly and therefore, the ratio between them (R_{GC}/R_e) remain the same. Therefore, the smaller R_{GC}/R_e of our UDGs compared to the R_{GC}/R_e in dwarf galaxies of similar total mass (based on their N_{GC}) disfavors these models.

Furthermore, models that allow for star formation after some critical event, such as a merger or strong feedback effect, might face challenges in maintaining the close correspondence of R_{GC} and R_e , as well as R_{GC}/R_e and the azimuthal alignment. These considerations place additional constraints on these models. Moreover, a slightly larger R_{GC} (about 1.5 times) of UDGs compared to the dwarf sample can be the indication of a secondary process or a more complicated model for UDG formation.

In Table 4 we have catalogued our understanding of how the models fare against these constraints, but caution the reader that specific predictions from the models are not yet available and we have taken our best guess. In addition, in some cases the models can probably be easily modified to address perceived challenges.

6 CONCLUSIONS

We present an analysis of six ultra-diffuse galaxies (UDG) and their globular clusters (GCs) to study the nature of GCs in UDGs and provide additional constraints on formation models of UDGs. The galaxy sample is comprised of UDGs with large effective radii ($\langle R_e \rangle \sim 3.6$ kpc) in the Coma galaxy cluster. We combine deep new and archival *HST* observations to identify GCs up to and fainter than the turnover of the GC luminosity function ($M_I \sim -8.1$ mag). We find that:

- The GC luminosity function (GCLF) is consistent with that of similar galaxies, with a turnover magnitude, $\mu_{\text{peak},814}$, of -8.14 ± 0.14 mag and a width, σ_{814} , of 0.79 ± 0.06 . The nature of the luminosity function is important to establish because the total GC count includes a correction for those GCs that are too faint to detect.

- The GC distribution, in both radius and azimuth, is consistent with that of the underlying stars. We find that the half number radius for GCs relative to the half light radius, R_{GC}/R_e , is $1.09^{+0.13}_{-0.14}$ and that the GC systems are also extended along the galaxy’s major axis. Understanding the distribution of GCs is critical because the total GC count includes a correction for those GCs that are at large radii and difficult to distinguish from contaminants.

- The number of GCs in each galaxy, N_{GC} , spans 10 to 30, with an average of ~ 21 GCs for each of our galaxies. We find no statistically convincing trend between UDG properties and N_{GC} , although this is not surprising because our sample was specifically selected to be composed of similar galaxies. We do find that all six galaxies lie at the upper end of the N_{GC} range for galaxies of similar stellar mass (about a factor of two larger than the mean) and well

within the scatter of galaxies with the same stellar mass.

- Adopting a relation between N_{GC} and total mass, M_{total} , we find that our UDGs have $M_{\text{total}} \sim 10^{11} M_{\odot}$ and that they have large M_{total}/M_* . The latter implies that these galaxies are relatively inefficient at forming field stars, while forming GCs at the standard rate. Confirming the $N_{GC}-M_{\text{total}}$ relationship with additional kinematic mass measurements is a priority.

- The lower ratio R_{GC}/R_e that we find for these UDGs (~ 1) compared to dwarf galaxies (~ 1.5) suggests that the process that is responsible for the larger R_e of UDGs does not have the same influence on the GC distribution: either it has a weaker effect or no effect. In the case of the latter, a secondary process might play a role in increasing the R_{GC} of UDGs.

- These findings disfavour UDG models that appeal primarily to a redistribution of the stars to larger radii to reduce a galaxy’s surface brightness and suggest that a decline in integrated star formation efficiency is needed. However, that decline should occur after GC formation, because the GC formation efficiency appears to have been normal. This would disfavour ‘intrinsic’ property models, such as that appealing to high-spin. Complex histories, with multiple star formation or dynamical events may be difficult to reconcile with the close spatial alignment of GCs and field stars in UDGs without invoking some fine tuning.

We look forward both to enlarging the sample of UDGs with high-fidelity GC measurements with which to test and extend the results presented here, and to comparisons of GC properties with UDG models specifically tailored to make predictions regarding GCs. Such comparisons have the potential to help us reach an accurate understanding of both UDG and GC formation. In the upcoming years, several wide-field surveys, including the ESA mission *Euclid*, observe hundreds of thousand of LSB galaxies, UDGs and their GCs in the Local Universe within 100 Mpc (Lançon et al. 2021), which provide a much deeper picture of LSBs/UDGs, their formation and evolution.

ACKNOWLEDGEMENTS

We thank the referee for a number of excellent suggestions to improve the quality of the paper. We would like to thank Scott Carlsten for sharing the data of the GCs around dwarf galaxies and his kind response to our queries. We thank Arianna Di Cintio for discussion on formation of UDGs, and Edwin Valentijn for his comments on this work. We thank Andrea Afruni for his help and assistance in developing the MLE code used in this work. T.S., R.P., J.H.K., I.T. acknowledge financial support from the European Union’s Horizon 2020 research and innovation programme under

Marie Skłodowska-Curie grant agreement No 721463 to the SUN-DIAL ITN network. D.Z. acknowledges support from NASA/STScI through NAS5-26555(HST-GO-15121.001-A), which also provided many of the observations used here. J.H.K. acknowledges financial support from the State Research Agency (AEI-MCINN) of the Spanish Ministry of Science and Innovation under the grant "The structure and evolution of galaxies and their central regions" with reference PID2019-105602GB-I00/10.13039/501100011033, from the ACIISI, Consejería de Economía, Conocimiento y Empleo del Gobierno de Canarias and the European Regional Development Fund (ERDF) under grant with reference PROID2021010044, and from IAC project P/300724, financed by the Ministry of Science and Innovation, through the State Budget and by the Canary Islands Department of Economy, Knowledge and Employment, through the Regional Budget of the Autonomous Community. N.C.A. is supported by an STFC/UKRI Ernest Rutherford Fellowship, Project Reference: ST/S004998/1. I.T. acknowledges financial support from the State Research Agency (AEI-MCINN) of the Spanish Ministry of Science and Innovation under the grant with reference PID2019-107427GB-C32, and from IAC project P/300624, financed by the Ministry of Science and Innovation, through the State Budget and by the Canary Islands Department of Economy, Knowledge and Employment, through the Regional Budget of the Autonomous Community. M.A.B acknowledges support from the grant PID2019-107427GB-C32 from the Spanish Ministry of Science, Innovation and Universities (MCIU) and from the Severo Ochoa Excellence scheme (SEV-2015-0548). This work has been backed through the IAC project TRACES which is partially supported through the state budget and the regional budget of the Consejería de Economía, Industria, Comercio y Conocimiento of the Canary Islands Autonomous Community. This research has made use of the SIMBAD database (Wenger et al. 2000), operated at CDS, Strasbourg, France, the Vizier catalogue access tool (Ochsenbein et al. 2000), CDS, Strasbourg, France (DOI: 10.26093/cds/vizier), and the Aladin sky atlas (Bonnarel et al. 2000; Boch & Fernique 2014) developed at CDS, Strasbourg Observatory, France and SAOImageDS9 (Joye & Mandel 2003). This work has been done using the following software, packages and PYTHON libraries: NUMPY (van der Walt et al. 2011), SCIPY (Virtanen et al. 2020), ASTROPY (Astropy Collaboration et al. 2018), SCIKIT-LEARN (Pedregosa et al. 2011).

DATA AVAILABILITY

The data underlying this article were retrieved from the Hubble Space Telescope archive and it provides the reduced/drizzled frames by the standard *HST* pipeline. The software and packages that are used in this work are publicly available. The catalogue of the Globular Cluster candidates around the UDG sample generated in this research are available in the article and its online supplementary material.

REFERENCES

- Amorisco N. C., 2018, *MNRAS*, **475**, L116
 Amorisco N. C., 2019, *MNRAS*, **489**, L22
 Amorisco N. C., Loeb A., 2016, *MNRAS*, **459**, L51
 Amorisco N. C., Monachesi A., Agnello A., White S. D. M., 2018, *MNRAS*, **475**, 4235
 Astropy Collaboration et al., 2018, *AJ*, **156**, 123
 Barbosa C. E., et al., 2020, *ApJS*, **247**, 46
 Bastian N., Pfeffer J., Kruijssen J. M. D., Crain R. A., Trujillo-Gomez S., Reina-Campos M., 2020, *MNRAS*, **498**, 1050
 Beasley M. A., Trujillo I., 2016, *ApJ*, **830**, 23
 Beasley M. A., Romanowsky A. J., Pota V., Navarro I. M., Martinez Delgado D., Neyer F., Deich A. L., 2016, *ApJ*, **819**, L20
 Benavides J. A., et al., 2021, *Nature Astronomy*, **5**, 1255
 Bertin E., Arnouts S., 1996, *A&AS*, **117**, 393
 Bertin E., Mellier Y., Radovich M., Missonnier G., Didelon P., Morin B., 2002, The TERAPIX Pipeline. p. 228
 Binggeli B., Sandage A., Tammann G. A., 1985, *AJ*, **90**, 1681
 Blakeslee J. P., et al., 2010, *ApJ*, **724**, 657
 Blanton M. R., Roweis S., 2007, *AJ*, **133**, 734
 Boch T., Fernique P., 2014, in Manset N., Forshay P., eds, *Astronomical Society of the Pacific Conference Series Vol. 485, Astronomical Data Analysis Software and Systems XXIII*. p. 277
 Bogdán Á., 2020, *ApJ*, **901**, L30
 Bonnarel F., et al., 2000, *A&AS*, **143**, 33
 Bothun G. D., Impey C. D., Malin D. F., 1991, *ApJ*, **376**, 404
 Boylan-Kolchin M., 2017, *MNRAS*, **472**, 3120
 Brodie J. P., Strader J., 2006, *ARA&A*, **44**, 193
 Carleton T., Errani R., Cooper M., Kaplinghat M., Peñarrubia J., Guo Y., 2019, *MNRAS*, **485**, 382
 Carleton T., Guo Y., Munshi F., Tremmel M., Wright A., 2021, *MNRAS*, **502**, 398
 Carlsten S. G., Greene J. E., Beaton R. L., Greco J. P., 2021, arXiv e-prints, p. arXiv:2105.03440
 Chan T. K., Kereš D., Wetzel A., Hopkins P. F., Faucher-Giguère C. A., El-Badry K., Garrison-Kimmel S., Boylan-Kolchin M., 2018, *MNRAS*, **478**, 906
 Chen H., et al., 2020, *MNRAS*, **496**, 4654
 Chilingarian I. V., Afanasiev A. V., Grishin K. A., Fabricant D., Moran S., 2019, *ApJ*, **884**, 79
 Danieli S., et al., 2021, arXiv e-prints, p. arXiv:2111.14851
 Di Cintio A., Brook C. B., Dutton A. A., Macciò A. V., Obreja A., Dekel A., 2017, *MNRAS*, **466**, L1
 Diemer B., 2018, *ApJS*, **239**, 35
 El-Badry K., Quataert E., Weisz D. R., Choksi N., Boylan-Kolchin M., 2019, *MNRAS*, **482**, 4528
 Erkal D., et al., 2019, *MNRAS*, **487**, 2685
 Ferré-Mateu A., et al., 2018, *MNRAS*, **479**, 4891
 Fliri J., Trujillo I., 2016, *MNRAS*, **456**, 1359
 Forbes D. A., Read J. I., Gieles M., Collins M. L. M., 2018, *MNRAS*, **481**, 5592
 Forbes D. A., Gannon J. S., Romanowsky A. J., Alabi A., Brodie J. P., Couch W. J., Ferré-Mateu A., 2021, *MNRAS*, **500**, 1279
 Freundlich J., Dekel A., Jiang F., Ishai G., Cornuault N., Lapiner S., Dutton A. A., Macciò A. V., 2020, *MNRAS*, **491**, 4523
 Gannon J. S., Forbes D. A., Romanowsky A. J., Ferré-Mateu A., Couch W. J., Brodie J. P., 2020, *MNRAS*, **495**, 2582
 Gannon J. S., et al., 2021, *MNRAS*,
 Gennaro, M., et al. 2018, *WFC3 Data Handbook, Version 4.0*, (Baltimore: STScI)
 Godwin J. G., Metcalfe N., Peach J. V., 1983, *MNRAS*, **202**, 113
 Gómez M., Richtler T., Infante L., Drenkhahn G., 2001, *A&A*, **371**, 875
 Gu M., et al., 2018, *ApJ*, **859**, 37
 Habas R., et al., 2020, *MNRAS*, **491**, 1901
 Harris W. E., 2018, *AJ*, **156**, 296
 Harris W. E., Kavelaars J. J., Hanes D. A., Pritchett C. J., Baum W. A., 2009, *AJ*, **137**, 3314
 Harris W. E., Harris G. L. H., Alessi M., 2013, *ApJ*, **772**, 82
 Harris W. E., et al., 2014, *ApJ*, **797**, 128
 Harris W. E., Blakeslee J. P., Harris G. L. H., 2017, *ApJ*, **836**, 67
 Impey C., Bothun G., 1997, *ARA&A*, **35**, 267
 Into T., Portinari L., 2013, *MNRAS*, **430**, 2715
 Iodice E., et al., 2020, *A&A*, **642**, A48
 Jensen J. B., Tonry J. L., Luppino G. A., 1999, *ApJ*, **510**, 71
 Jiang F., Dekel A., Freundlich J., Romanowsky A. J., Dutton A. A., Macciò A. V., Di Cintio A., 2019, *MNRAS*, **487**, 5272
 Jones M. G., Papastergis E., Pandya V., Leisman L., Romanowsky A. J., Yung L. Y. A., Somerville R. S., Adams E. A. K., 2018, *A&A*, **614**, A21

- Jones M. G., Bennet P., Mutlu-Pakdil B., Sand D. J., Spekkens K., Crnojević D., Karunakaran A., Zaritsky D., 2021, *ApJ*, 919, 72
- Jordán A., et al., 2007, *ApJS*, 171, 101
- Jordán A., Peng E. W., Blakeslee J. P., Côté P., Eyheramendy S., Ferrarese L., 2015, *ApJS*, 221, 13
- Joye W. A., Mandel E., 2003, in Payne H. E., Jedrzejewski R. I., Hook R. N., eds, *Astronomical Society of the Pacific Conference Series Vol. 295, Astronomical Data Analysis Software and Systems XII*. p. 489
- Kado-Fong E., et al., 2021, *ApJ*, 920, 72
- Kadowaki J., Zaritsky D., Donnerstein R. L., 2017, *ApJ*, 838, L21
- Kadowaki J., Zaritsky D., Donnerstein R. L., RSP, Karunakaran A., Spekkens K., 2021, *ApJ*, 923, 257
- Karunakaran A., Spekkens K., Zaritsky D., Donnerstein R. L., Kadowaki J., Dey A., 2020, *ApJ*, 902, 39
- Kavelaars J. J., 1998, *PASP*, 110, 758
- Kissler-Patig M., Richtler T., Storm J., della Valle M., 1997, *A&A*, 327, 503
- Koda J., Yagi M., Yamanoi H., Komiyama Y., 2015, *ApJ*, 807, L2
- Kruijssen J. M. D., Pfeffer J. L., Crain R. A., Bastian N., 2019, *MNRAS*, 486, 3134
- Kubo J. M., Stebbins A., Annis J., Dell’Antonio I. P., Lin H., Khiabani H., Frieman J. A., 2007, *ApJ*, 671, 1466
- Kundu A., Whitmore B. C., 2001, *AJ*, 121, 2950
- Lançon A., et al., 2021, in Siebert A., et al., eds, *SF2A-2021: Proceedings of the Annual meeting of the French Society of Astronomy and Astrophysics*. pp 447–450 ([arXiv: 2110.13783](https://arxiv.org/abs/2110.13783))
- Lee C. H., Hodges-Kluck E., Gallo E., 2020, *MNRAS*, 497, 2759
- Leisman L., et al., 2017, *ApJ*, 842, 133
- Liao S., et al., 2019, *MNRAS*, 490, 5182
- Lim S., Peng E. W., Côté P., Sales L. V., den Brok M., Blakeslee J. P., Guhathakurta P., 2018, *ApJ*, 862, 82
- Lim S., et al., 2020, *ApJ*, 899, 69
- Liu Y., Peng E. W., Jordán A., Blakeslee J. P., Côté P., Ferrarese L., Puzia T. H., 2019, *ApJ*, 875, 156
- Mancera Piña P. E., Aguerri J. A. L., Peletier R. F., Venhola A., Trager S., Choque Challapa N., 2019, *MNRAS*, 485, 1036
- Mancera Piña P. E., et al., 2020, *MNRAS*, 495, 3636
- Marleau F. R., et al., 2021, *A&A*, 654, A105
- Martin G., et al., 2019, *MNRAS*, 485, 796
- Miller B. W., Lotz J. M., 2007, *ApJ*, 670, 1074
- Montes M., Trujillo I., Infante-Sainz R., Monelli M., Borlaff A. S., 2021, *ApJ*, 919, 56
- Müller O., et al., 2020, *A&A*, 640, A106
- Müller O., et al., 2021, *ApJ*, 923, 9
- Navarro J. F., Eke V. R., Frenk C. S., 1996, *MNRAS*, 283, L72
- Ochsenbein F., Bauer P., Marcout J., 2000, *A&AS*, 143, 23
- Pandya V., et al., 2018, *ApJ*, 858, 29
- Papastergis E., Adams E. A. K., Romanowsky A. J., 2017, *A&A*, 601, L10
- Pedregosa F., et al., 2011, *Journal of Machine Learning Research*, 12, 2825
- Peng E. W., Lim S., 2016, *ApJ*, 822, L31
- Peng C. Y., Ho L. C., Impey C. D., Rix H.-W., 2002, *AJ*, 124, 266
- Peng E. W., et al., 2006, *ApJ*, 639, 95
- Peng E. W., et al., 2008, *ApJ*, 681, 197
- Peng C. Y., Ho L. C., Impey C. D., Rix H.-W., 2010, *AJ*, 139, 2097
- Pfeffer J., Kruijssen J. M. D., Crain R. A., Bastian N., 2018, *MNRAS*, 475, 4309
- Pontzen A., Governato F., 2012, *MNRAS*, 421, 3464
- Poulain M., et al., 2021, *arXiv e-prints*, [p. arXiv:2111.14491](https://arxiv.org/abs/2111.14491)
- Prole D. J., Davies J. I., Keenan O. C., Davies L. J. M., 2018, *MNRAS*, 478, 667
- Prole D. J., van der Burg R. F. J., Hilker M., Davies J. I., 2019, *MNRAS*, 488, 2143
- Prole D. J., van der Burg R. F. J., Hilker M., Spitler L. R., 2021, *MNRAS*, 500, 2049
- Rejkuba M., 2012, *Ap&SS*, 341, 195
- Román J., Trujillo I., 2017, *MNRAS*, 468, 4039
- Román J., Beasley M. A., Ruiz-Lara T., Valls-Gabaud D., 2019, *MNRAS*, 486, 823
- Román J., Castilla A., Pascual-Granado J., 2021, *A&A*, 656, A44
- Rong Y., et al., 2020, *ApJ*, 899, 78
- Ruiz-Lara T., et al., 2018, *MNRAS*, 478, 2034
- Saifollahi T., Trujillo I., Beasley M. A., Peletier R. F., Knapen J. H., 2021, *MNRAS*, 502, 5921
- Sales L. V., Navarro J. F., Peñafiel L., Peng E. W., Lim S., Hernquist L., 2020, *MNRAS*, 494, 1848
- Secker J., Harris W. E., 1993, *AJ*, 105, 1358
- Sengupta C., Scott T. C., Chung A., Wong O. I., 2019, *MNRAS*, 488, 3222
- Sifón C., van der Burg R. F. J., Hoekstra H., Muzzin A., Herbonnet R., 2018, *MNRAS*, 473, 3747
- Singh P. R., Zaritsky D., Donnerstein R., Spekkens K., 2019, *AJ*, 157, 212
- Somalwar J. J., Greene J. E., Greco J. P., Huang S., Beaton R. L., Goulding A. D., Lancaster L., 2020, *ApJ*, 902, 45
- Spekkens K., Karunakaran A., 2018, *ApJ*, 855, 28
- Struble M. F., Rood H. J., 1999, *ApJS*, 125, 35
- Thomsen B., Baum W. A., Hammergren M., Worthey G., 1997, *ApJ*, 483, L37
- Toloba E., et al., 2018, *ApJ*, 856, L31
- Tremmel M., Wright A. C., Brooks A. M., Munshi F., Nagai D., Quinn T. R., 2020, *MNRAS*, 497, 2786
- Trujillo-Gomez S., Kruijssen J. M. D., Reina-Campos M., 2022, *MNRAS*, 510, 3356
- Trujillo I., Graham A. W., Caon N., 2001, *MNRAS*, 326, 869
- Trujillo I., Roman J., Filho M., Sánchez Almeida J., 2017, *ApJ*, 836, 191
- Trujillo I., et al., 2021, *A&A*, 654, A40
- Valenzuela L. M., Moster B. P., Remus R.-S., O’Leary J. A., Burkert A., 2021, *MNRAS*, 505, 5815
- Van Nest J. D., Munshi F., Wright A. C., Tremmel M., Brooks A. M., Nagai D., Quinn T., 2021, *arXiv e-prints*, [p. arXiv:2108.12985](https://arxiv.org/abs/2108.12985)
- Vazdekis A., Sánchez-Blázquez P., Falcón-Barroso J., Cenarro A. J., Beasley M. A., Cardiel N., Gorgas J., Peletier R. F., 2010, *MNRAS*, 404, 1639
- Vazdekis A., Koleva M., Ricciardelli E., Röck B., Falcón-Barroso J., 2016, *MNRAS*, 463, 3409
- Venhola A., et al., 2017, *A&A*, 608, A142
- Villaume A., et al., 2022, *ApJ*, 924, 32
- Virtanen P., et al., 2020, *Nature Methods*, 17, 261
- Wenger M., et al., 2000, *A&AS*, 143, 9
- Wright A. C., Tremmel M., Brooks A. M., Munshi F., Nagai D., Sharma R. S., Quinn T. R., 2021, *MNRAS*, 502, 5370
- Yagi M., Koda J., Komiyama Y., Yamanoi H., 2016, *ApJS*, 225, 11
- Yozin C., Bekki K., 2015, *MNRAS*, 452, 937
- Zaritsky D., 2017, *MNRAS*, 464, L110
- Zaritsky D., et al., 2019, *ApJS*, 240, 1
- Zaritsky D., Donnerstein R., Karunakaran A., Barbosa C. E., Dey A., Kadowaki J., Spekkens K., Zhang H., 2021, *ApJS*, 257, 60
- van Dokkum P. G., 2001, *PASP*, 113, 1420
- van Dokkum P. G., Abraham R., Merritt A., Zhang J., Geha M., Conroy C., 2015a, *ApJ*, 798, L45
- van Dokkum P. G., et al., 2015b, *ApJ*, 804, L26
- van Dokkum P., et al., 2016, *ApJ*, 828, L6
- van Dokkum P., et al., 2017, *ApJ*, 844, L11
- van Dokkum P., et al., 2019, *ApJ*, 880, 91
- van der Walt S., Colbert S. C., Varoquaux G., 2011, *Computing in Science and Engineering*, 13, 22

APPENDIX A: SÉRSIC MODELS AND PROFILES, GC SELECTION USING COMPACTNESS AND COLOUR, COMPLETENESS FUNCTIONS

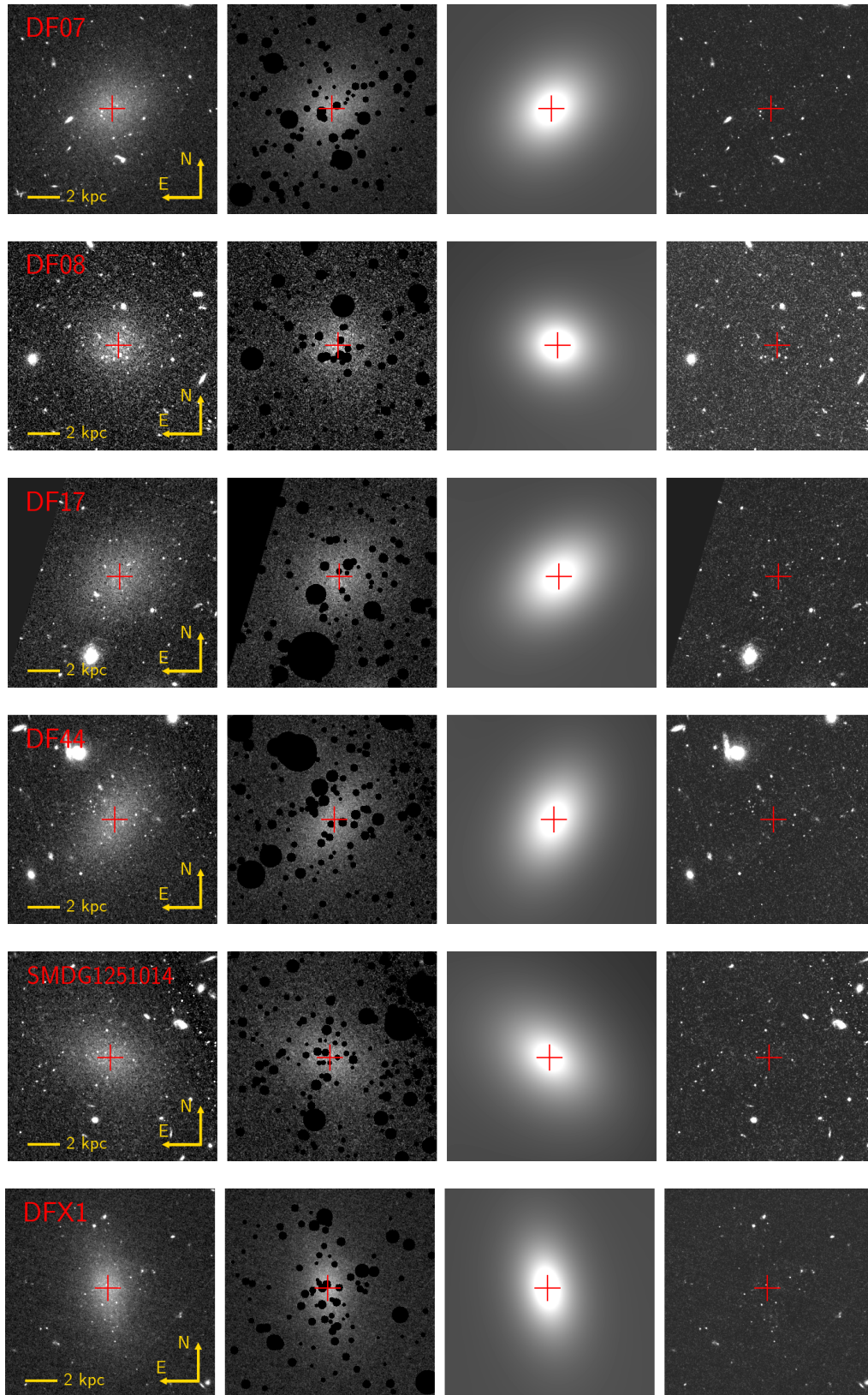


Figure A1. Modeling the light profile of the galaxies with a Sérsic profile in their primary filter. From left to right: the galaxy frame, the mask frame, the galaxy model and the residuals after subtracting the model from the main frame.

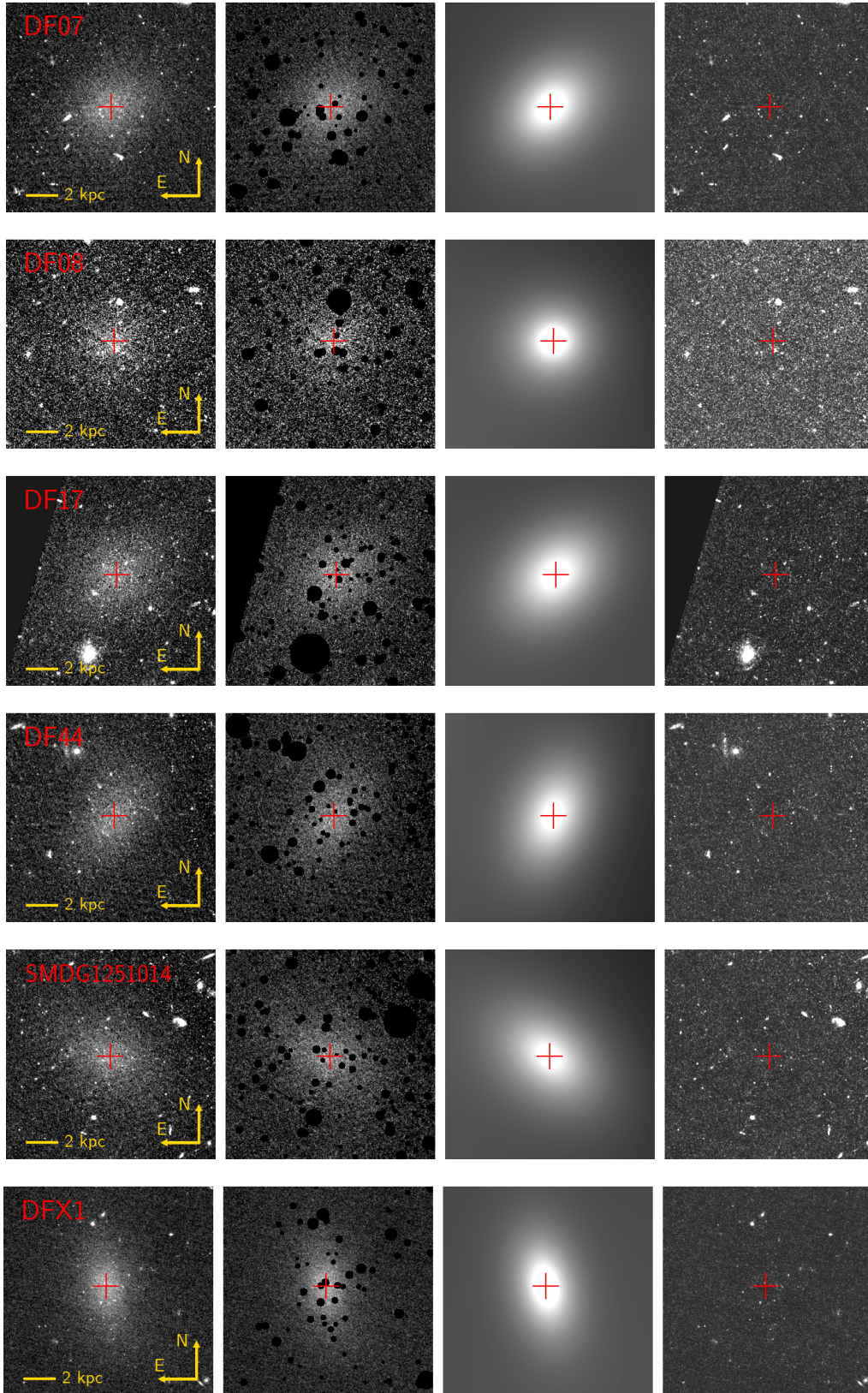


Figure A2. As Fig. A1, now for the secondary filter.

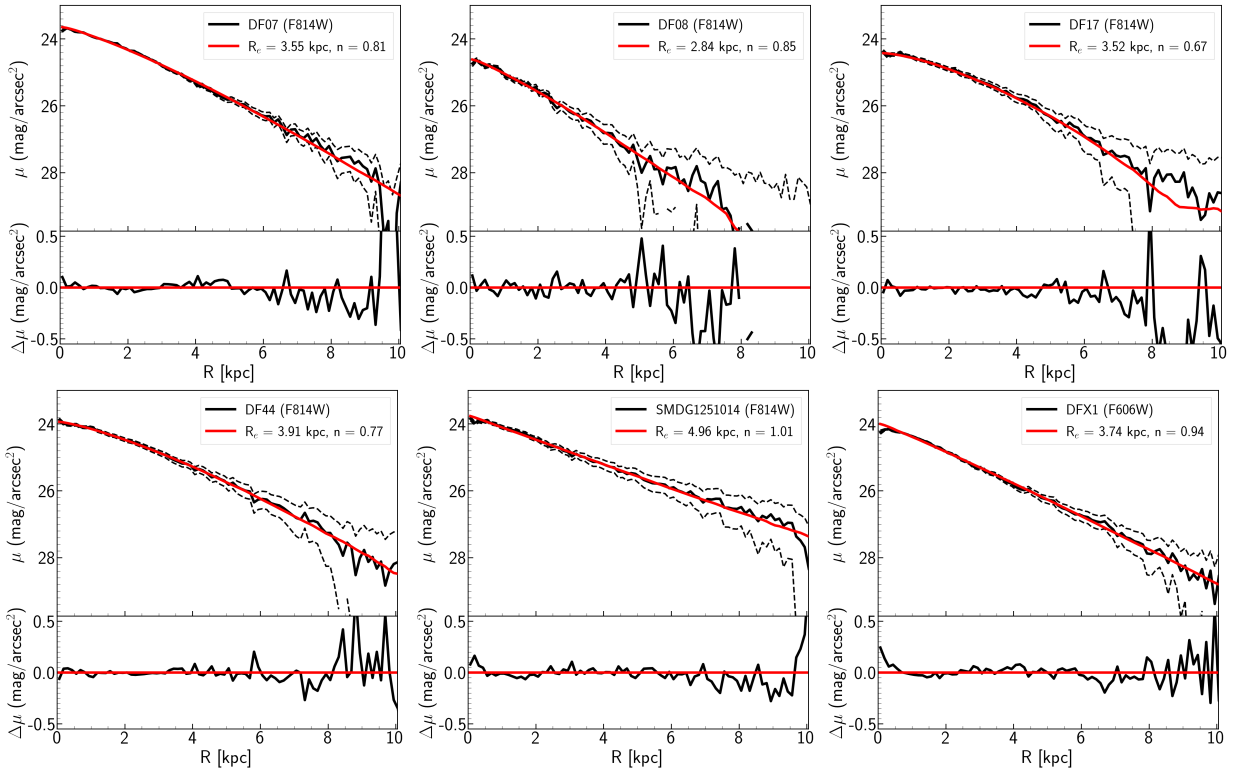


Figure A3. Sérsic profiles of the UDG sample in their primary filter. The light profile, best-fit Sérsic function for UDGs and fitting residuals. The black dashed lines indicate the 1-sigma uncertainty of the light profile.

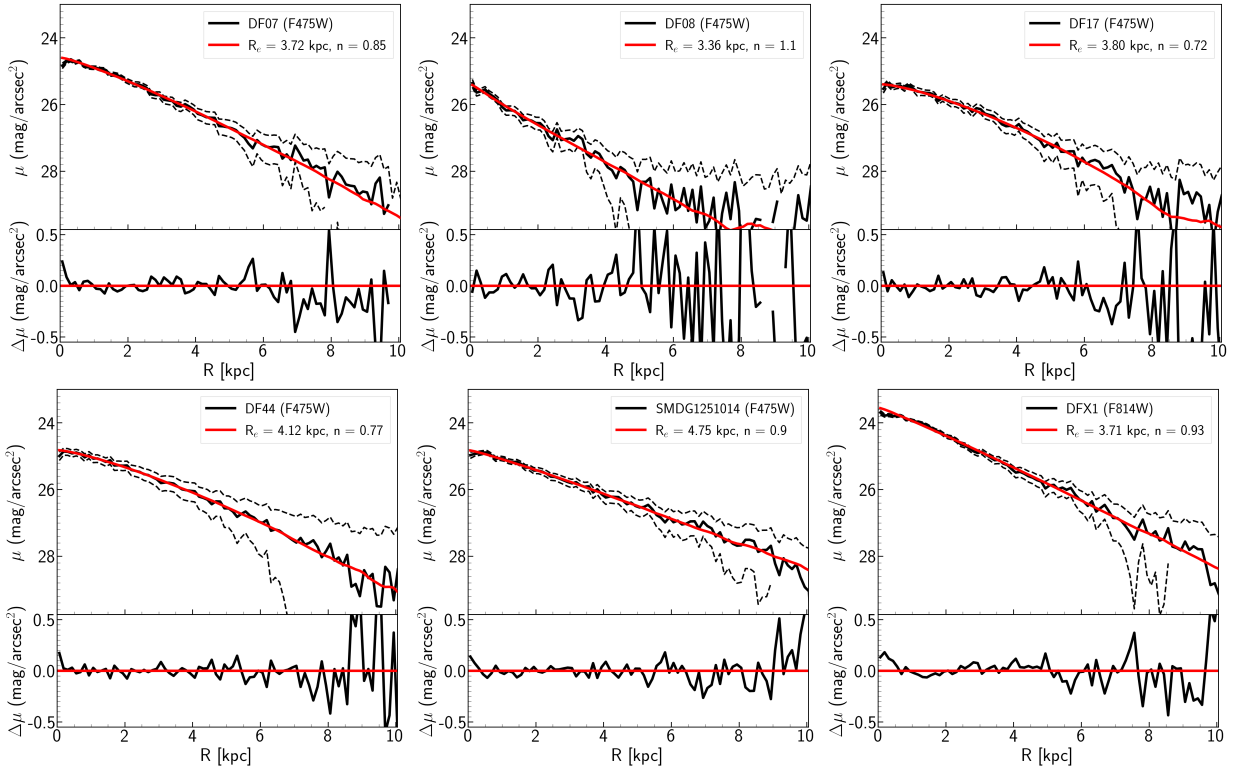


Figure A4. As Fig. A3, now for the secondary filter.

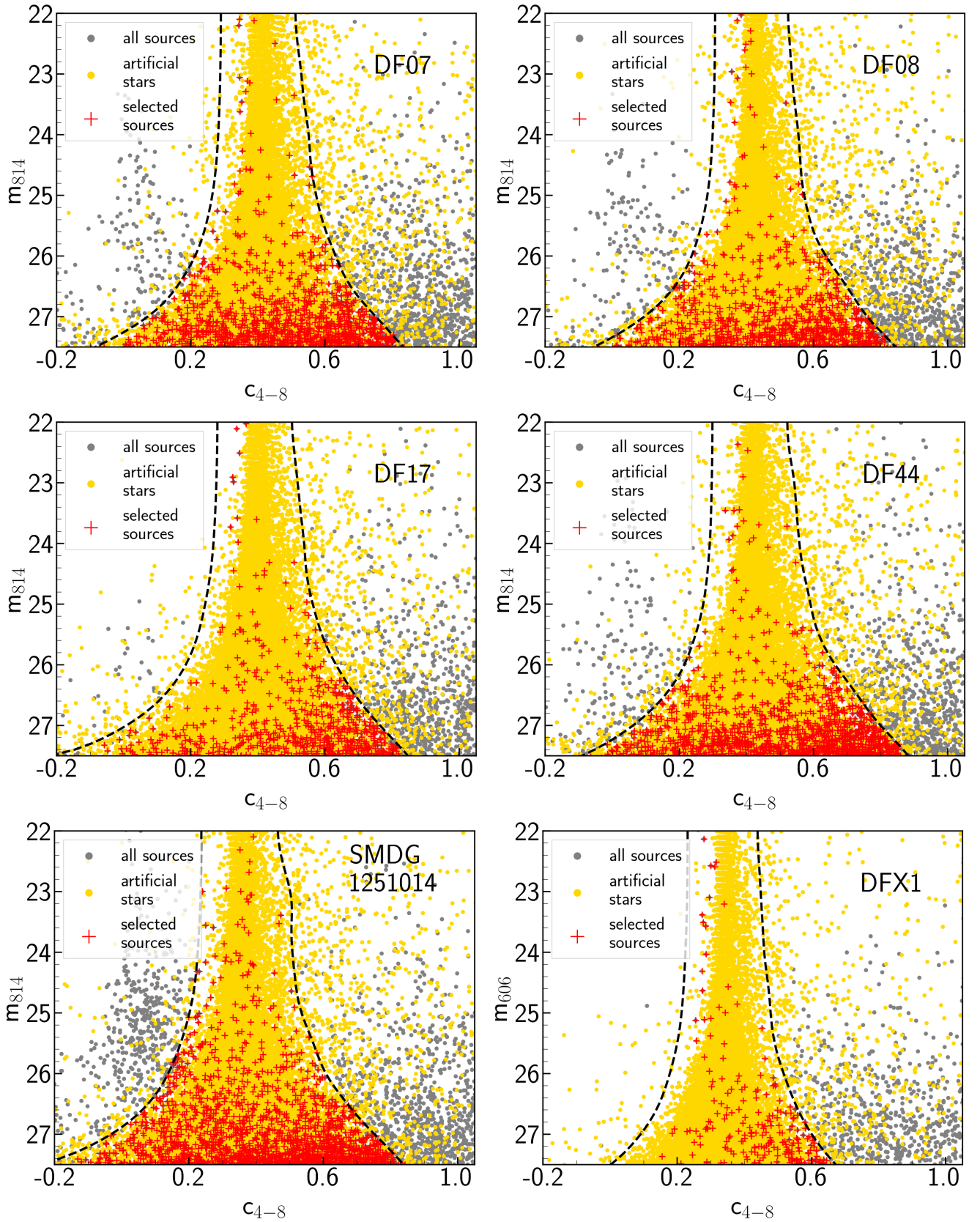


Figure A5. Compactness index (c_{4-8}) - magnitude diagram for the primary frames (six primary frames for six galaxies). The boundaries of point source selection are indicated with black dashed lines. All the sources in the primary frames, simulated stars and selected point sources are shown in grey dots, yellow dots and red crosses, respectively.

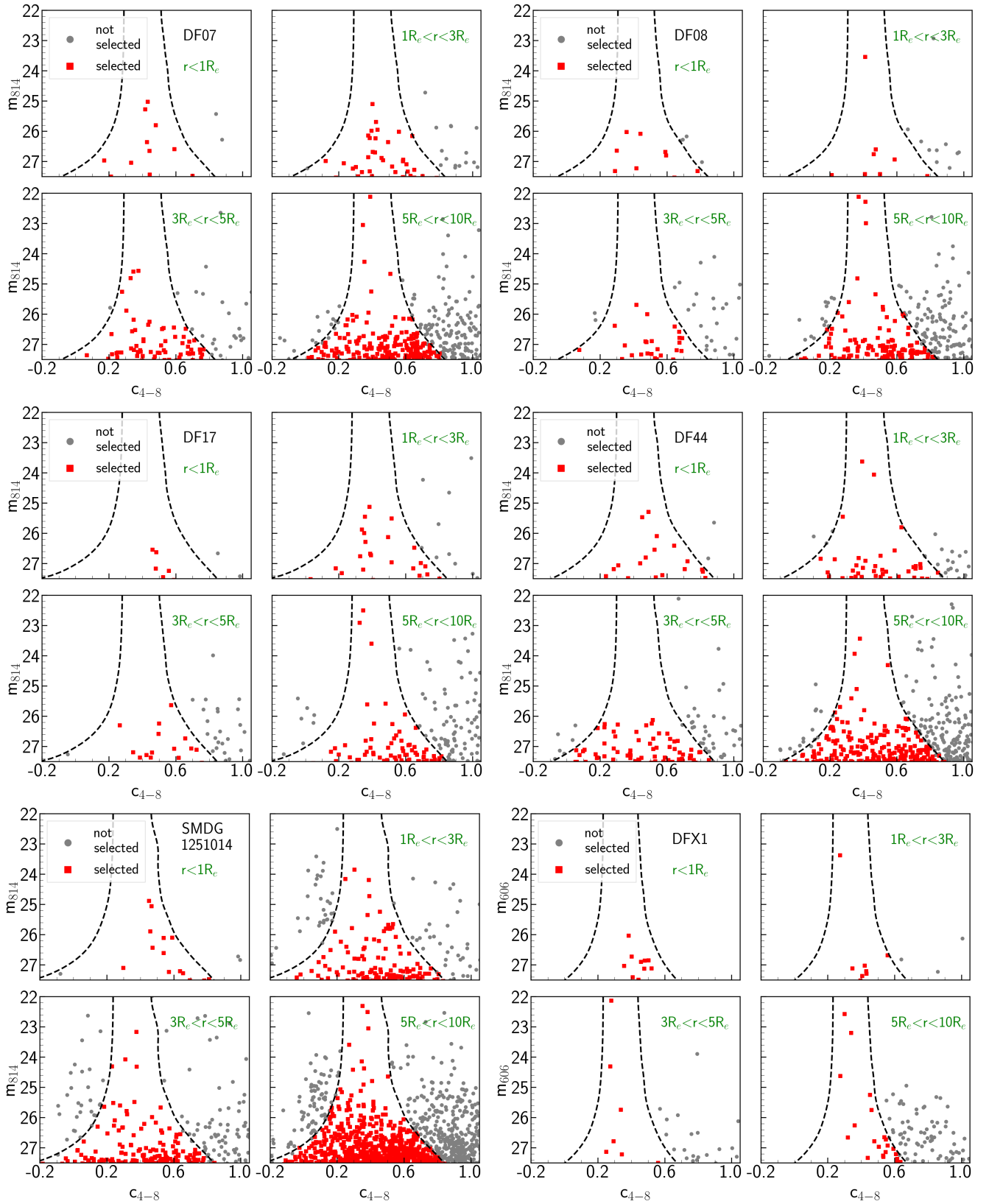


Figure A6. Similar diagram as the Fig. A5 for sources within different radial distances. The boundaries of point source selection are indicated with black dashed lines. Selected and not selected (discarded) sources are shown in red and grey dots, respectively.

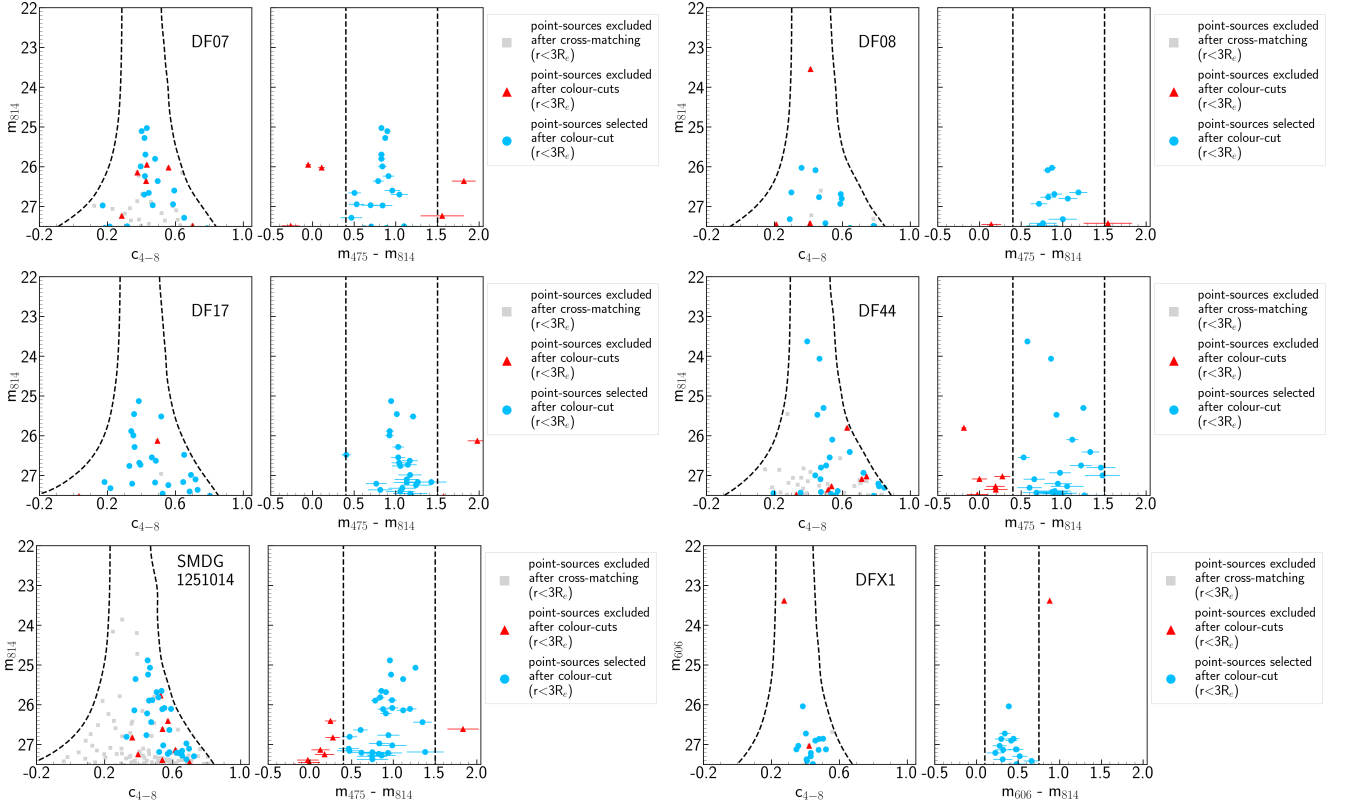


Figure A7. Compactness index (c_{4-8}) - magnitude diagram (left) and colour-magnitude diagram (right) of the selected point sources around the UDG samples and within $3R_e$ from the host galaxies.

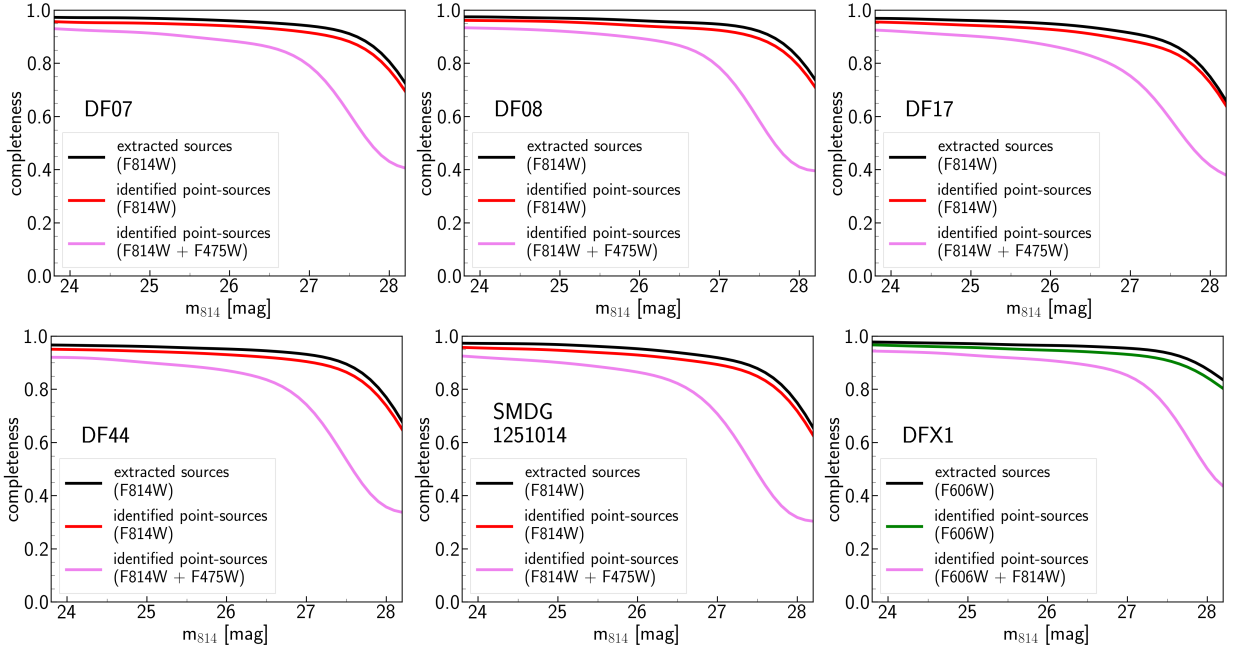


Figure A8. The completeness of source extraction (black), point source selection (red for $F814W$ primary filter and green for $F606W$ primary filter) and source selection after including the secondary filter (shallower data, purple), for the dataset corresponding to each galaxy.

APPENDIX B: CATALOGUES OF GC CANDIDATES

Table B1: GC candidates around UDGs. Columns from left to right represent host galaxy name, R.A., declination, distance from the host galaxy, magnitude in $F475W$ ($F606W$ for DFX1) and $F814W$, and compactness index in the primary filter. Quoted errors of magnitudes and compactness are statistical ones, systematic errors are not included.

Host Galaxy	RA	DEC	R	m_{475}	m_{814}	c_{4-8}
-	hms	dms	arcsec	AB mag	AB mag	AB mag
DF07	12h 57m 01.692s	+28d 23m 20.530s	4.47	25.85±0.02	25.03±0.01	0.43±0.02
DF07	12h 57m 01.113s	+28d 23m 30.033s	10.14	26.00±0.02	25.10±0.01	0.40±0.02
DF07	12h 57m 01.826s	+28d 23m 24.568s	1.94	26.15±0.03	25.28±0.02	0.42±0.03
DF07	12h 57m 01.361s	+28d 23m 18.061s	8.60	26.52±0.03	25.69±0.02	0.42±0.03
DF07	12h 57m 01.831s	+28d 23m 23.933s	2.23	26.63±0.04	25.80±0.02	0.48±0.04
DF07	12h 57m 00.862s	+28d 23m 34.287s	15.62	26.83±0.04	25.99±0.03	0.40±0.04
DF07	12h 57m 02.080s	+28d 23m 20.593s	7.21	27.15±0.06	26.23±0.03	0.42±0.06
DF07	12h 57m 00.942s	+28d 23m 28.155s	11.78	27.15±0.06	26.36±0.04	0.49±0.06
DF07	12h 57m 01.648s	+28d 23m 25.442s	0.88	27.55±0.08	26.60±0.05	0.59±0.07
DF07	12h 57m 01.797s	+28d 23m 23.448s	2.13	27.16±0.06	26.66±0.05	0.44±0.08
DF07	12h 57m 00.836s	+28d 23m 27.157s	13.12	27.74±0.09	26.70±0.05	0.42±0.08
DF07	12h 57m 01.314s	+28d 23m 13.434s	12.92	27.47±0.07	26.94±0.06	0.59±0.09
DF07	12h 57m 02.503s	+28d 23m 18.804s	13.55	27.66±0.09	26.97±0.06	0.46±0.10
DF07	12h 57m 01.317s	+28d 23m 26.361s	5.89	27.81±0.10	26.97±0.06	0.17±0.12
DF07	12h 57m 02.155s	+28d 23m 20.797s	8.01	27.75±0.10	27.28±0.08	0.65±0.12
DF07	12h 57m 02.252s	+28d 23m 31.150s	10.32	28.60±0.20	27.50±0.10	0.32±0.18
DF07	12h 57m 01.414s	+28d 23m 21.387s	5.60	28.21±0.14	27.50±0.10	0.21±0.19

Host galaxy	RA	DEC	R	m_{475}	m_{814}	c_{4-8}
-	hms	dms	arcsec	AB mag	AB mag	AB mag
DF08	13h 01m 30.226s	+28d 22m 23.748s	4.98	26.90±0.04	26.03±0.03	0.36±0.04
DF08	13h 01m 30.473s	+28d 22m 26.255s	2.06	26.91±0.04	26.09±0.03	0.44±0.05
DF08	13h 01m 30.255s	+28d 22m 30.810s	3.54	27.83±0.10	26.65±0.05	0.30±0.08
DF08	13h 01m 30.311s	+28d 22m 28.775s	1.53	27.59±0.08	26.69±0.05	0.59±0.07
DF08	13h 01m 29.987s	+28d 22m 25.159s	6.80	27.59±0.08	26.76±0.05	0.46±0.08
DF08	13h 01m 30.743s	+28d 22m 28.009s	5.15	27.86±0.10	26.80±0.05	0.59±0.08
DF08	13h 01m 29.834s	+28d 22m 24.806s	9.06	27.65±0.08	26.93±0.06	0.59±0.09
DF08	13h 01m 30.756s	+28d 22m 29.126s	5.46	28.32±0.15	27.32±0.08	0.29±0.14
DF08	13h 01m 30.165s	+28d 22m 38.834s	11.39	28.18±0.14	27.42±0.09	0.50±0.14
DF08	13h 01m 29.715s	+28d 22m 28.620s	10.28	28.21±0.14	27.49±0.09	0.78±0.13

Host Galaxy	RA	DEC	R	m_{475}	m_{814}	c_{4-8}
-	hms	dms	arcsec	AB mag	AB mag	AB mag
DF17	13h 01m 59.118s	+27d 50m 12.841s	12.41	26.07±0.02	25.13±0.01	0.38±0.02
DF17	13h 01m 57.526s	+27d 50m 14.550s	12.13	26.47±0.03	25.45±0.02	0.36±0.03
DF17	13h 01m 57.718s	+27d 50m 14.608s	9.43	26.72±0.04	25.51±0.02	0.52±0.03
DF17	13h 01m 58.405s	+27d 50m 05.476s	5.74	26.81±0.04	25.88±0.02	0.34±0.04
DF17	13h 01m 58.332s	+27d 50m 17.286s	6.30	26.91±0.04	25.99±0.03	0.35±0.04
DF17	13h 01m 57.537s	+27d 50m 16.736s	12.79	27.31±0.06	26.29±0.03	0.36±0.06
DF17	13h 01m 57.746s	+27d 49m 58.905s	14.67	26.88±0.04	26.48±0.04	0.65±0.06
DF17	13h 01m 58.397s	+27d 50m 07.170s	4.09	27.57±0.07	26.54±0.04	0.46±0.07
DF17	13h 01m 58.541s	+27d 50m 08.186s	4.59	27.80±0.09	26.63±0.04	0.48±0.07
DF17	13h 01m 58.984s	+27d 50m 04.670s	12.05	27.72±0.08	26.68±0.05	0.39±0.07
DF17	13h 01m 57.744s	+27d 50m 05.557s	9.95	27.87±0.10	26.73±0.05	0.39±0.08
DF17	13h 01m 57.841s	+27d 50m 15.961s	8.48	27.81±0.09	26.76±0.05	0.33±0.09
DF17	13h 01m 57.809s	+27d 50m 06.634s	8.55	28.16±0.13	26.99±0.06	0.69±0.08
DF17	13h 01m 57.276s	+27d 50m 06.796s	15.91	28.23±0.13	27.10±0.07	0.72±0.09

DF17	13h 01m 57.977s	+27d 50m 21.703s	11.74	28.43±0.15	27.16±0.07	0.18±0.12
DF17	13h 01m 58.258s	+27d 50m 17.415s	6.44	28.59±0.17	27.17±0.07	0.65±0.10
DF17	13h 01m 58.059s	+27d 50m 14.057s	4.73	28.30±0.14	27.17±0.07	0.48±0.11
DF17	13h 01m 57.703s	+27d 50m 12.062s	9.01	27.97±0.10	27.21±0.07	0.34±0.12
DF17	13h 01m 58.223s	+27d 50m 12.570s	1.94	28.48±0.16	27.24±0.08	0.56±0.12
DF17	13h 01m 57.885s	+27d 50m 11.882s	6.28	28.39±0.15	27.32±0.08	0.22±0.15
DF17	13h 01m 58.042s	+27d 50m 04.862s	7.25	28.17±0.12	27.36±0.08	0.73±0.11
DF17	13h 01m 59.039s	+27d 50m 02.486s	13.98	28.46±0.15	27.40±0.08	0.68±0.12
DF17	13h 01m 58.191s	+27d 50m 09.678s	2.10	28.63±0.18	27.45±0.09	0.52±0.14
DF17	13h 01m 58.265s	+27d 50m 01.057s	9.95	28.69±0.19	27.50±0.09	0.80±0.12

Host Galaxy	RA	DEC	R	m_{475}	m_{814}	c_{4-8}
-	hms	dms	arcsec	AB mag	AB mag	AB mag
DF44	13h 00m 58.365s	+26d 58m 26.645s	9.99	24.20±0.01	23.63±0.01	0.39±0.01
DF44	13h 00m 58.417s	+26d 58m 53.848s	19.86	24.92±0.01	24.06±0.01	0.46±0.01
DF44	13h 00m 57.734s	+26d 58m 35.624s	4.03	26.54±0.04	25.30±0.02	0.49±0.03
DF44	13h 00m 58.255s	+26d 58m 37.673s	4.66	26.40±0.03	25.47±0.02	0.45±0.03
DF44	13h 00m 58.217s	+26d 58m 36.120s	3.44	27.21±0.06	26.10±0.03	0.54±0.05
DF44	13h 00m 57.628s	+26d 58m 32.418s	6.13	27.74±0.10	26.41±0.04	0.64±0.06
DF44	13h 00m 57.750s	+26d 58m 34.088s	3.84	27.07±0.06	26.54±0.05	0.52±0.07
DF44	13h 00m 57.756s	+26d 58m 42.759s	8.57	27.96±0.12	26.75±0.06	0.50±0.09
DF44	13h 00m 58.018s	+26d 58m 34.187s	0.85	28.26±0.16	26.80±0.06	0.47±0.09
DF44	13h 00m 58.130s	+26d 58m 31.265s	4.21	27.90±0.11	26.93±0.07	0.72±0.09
DF44	13h 00m 58.211s	+26d 58m 36.856s	3.66	28.47±0.20	27.00±0.07	0.44±0.11
DF44	13h 00m 57.729s	+26d 58m 38.936s	5.65	27.75±0.10	27.09±0.08	0.47±0.12
DF44	13h 00m 57.798s	+26d 58m 30.938s	5.06	28.15±0.15	27.21±0.08	0.81±0.11
DF44	13h 00m 57.988s	+26d 58m 39.473s	4.47	28.32±0.17	27.27±0.09	0.81±0.13
DF44	13h 00m 57.344s	+26d 58m 23.378s	15.22	27.91±0.12	27.31±0.09	0.84±0.12
DF44	13h 00m 58.175s	+26d 58m 38.665s	4.51	28.29±0.17	27.39±0.10	0.57±0.15
DF44	13h 00m 58.097s	+26d 58m 48.583s	13.66	28.28±0.16	27.41±0.10	0.47±0.16
DF44	13h 00m 59.127s	+26d 58m 39.782s	17.57	28.11±0.14	27.43±0.09	0.35±0.16
DF44	13h 00m 57.765s	+26d 58m 27.948s	7.88	28.40±0.18	27.44±0.10	0.19±0.19
DF44	13h 00m 58.199s	+26d 58m 35.660s	3.06	28.36±0.18	27.46±0.10	0.53±0.16
DF44	13h 00m 58.536s	+26d 58m 25.958s	12.10	28.76±0.24	27.50±0.10	0.56±0.15
DF44	13h 00m 57.537s	+26d 58m 32.334s	7.42	28.50±0.20	27.50±0.11	0.78±0.15

Host Galaxy	RA	DEC	R	m_{475}	m_{814}	c_{4-8}
-	hms	dms	arcsec	AB mag	AB mag	AB mag
SMDG1251014	12h 51m 01.366s	+27d 47m 56.849s	3.97	25.84±0.02	24.88±0.01	0.45±0.02
SMDG1251014	12h 51m 01.486s	+27d 47m 48.510s	5.29	26.33±0.03	25.07±0.02	0.47±0.02
SMDG1251014	12h 51m 01.791s	+27d 47m 33.136s	21.18	26.21±0.03	25.24±0.02	0.45±0.03
SMDG1251014	12h 51m 02.361s	+27d 47m 41.343s	19.73	26.47±0.03	25.35±0.02	0.38±0.03
SMDG1251014	12h 51m 00.677s	+27d 47m 46.748s	11.23	26.51±0.03	25.65±0.02	0.53±0.04
SMDG1251014	12h 51m 02.141s	+27d 47m 51.386s	12.72	26.59±0.03	25.68±0.02	0.50±0.04
SMDG1251014	12h 51m 00.194s	+27d 47m 46.506s	17.80	26.66±0.04	25.81±0.03	0.52±0.05
SMDG1251014	12h 51m 01.874s	+27d 47m 53.512s	8.62	26.87±0.05	25.88±0.03	0.48±0.04
SMDG1251014	12h 51m 01.471s	+27d 47m 53.577s	2.63	26.68±0.04	25.90±0.03	0.46±0.05
SMDG1251014	12h 51m 00.150s	+27d 47m 44.684s	19.14	27.07±0.05	26.08±0.04	0.55±0.06
SMDG1251014	12h 51m 01.059s	+27d 47m 52.332s	3.66	27.30±0.07	26.10±0.04	0.59±0.05
SMDG1251014	12h 51m 00.818s	+27d 47m 58.577s	9.12	26.98±0.05	26.11±0.04	0.54±0.06
SMDG1251014	12h 51m 01.636s	+27d 47m 58.326s	7.34	27.26±0.06	26.14±0.04	0.37±0.06
SMDG1251014	12h 51m 02.334s	+27d 47m 47.917s	16.33	27.12±0.05	26.22±0.04	0.45±0.06
SMDG1251014	12h 51m 01.381s	+27d 47m 53.445s	1.30	27.79±0.10	26.44±0.05	0.47±0.08
SMDG1251014	12h 51m 00.977s	+27d 48m 04.059s	12.07	27.24±0.07	26.63±0.05	0.58±0.08
SMDG1251014	12h 51m 00.608s	+27d 47m 59.469s	12.22	27.71±0.11	26.77±0.07	0.45±0.12
SMDG1251014	12h 51m 00.696s	+27d 47m 51.682s	9.14	27.28±0.07	26.81±0.06	0.33±0.11
SMDG1251014	12h 51m 02.061s	+27d 47m 36.847s	19.78	27.80±0.10	26.97±0.07	0.68±0.10

SMDG1251014	12h 51m 00.659s	+27d 48m 06.908s	16.90	28.01±0.14	27.02±0.09	0.54±0.14
SMDG1251014	12h 51m 00.434s	+27d 47m 48.927s	13.61	27.57±0.08	27.10±0.09	0.70±0.12
SMDG1251014	12h 51m 00.193s	+27d 48m 02.504s	19.12	27.63±0.10	27.15±0.11	0.66±0.16
SMDG1251014	12h 51m 01.293s	+27d 48m 01.670s	8.67	28.57±0.20	27.19±0.09	0.52±0.14
SMDG1251014	12h 51m 01.004s	+27d 47m 36.604s	16.98	27.94±0.12	27.20±0.09	0.58±0.14
SMDG1251014	12h 51m 01.635s	+27d 47m 44.250s	10.09	27.82±0.10	27.20±0.09	0.62±0.13
SMDG1251014	12h 51m 01.200s	+27d 47m 38.733s	14.34	28.15±0.14	27.21±0.09	0.63±0.14
SMDG1251014	12h 51m 01.137s	+27d 47m 53.285s	2.44	28.06±0.13	27.24±0.10	0.57±0.15
SMDG1251014	12h 51m 01.238s	+27d 47m 52.692s	0.96	28.13±0.14	27.28±0.10	0.65±0.15
SMDG1251014	12h 51m 00.665s	+27d 47m 59.074s	11.28	28.04±0.14	27.29±0.11	0.72±0.16
SMDG1251014	12h 51m 00.128s	+27d 48m 04.576s	21.04	28.12±0.14	27.37±0.12	0.68±0.17

Host Galaxy	RA	DEC	R	m_{606}	m_{814}	c_{4-8}
-	hms	dms	arcsec	AB mag	AB mag	AB mag
DFX1	13h 01m 15.894s	+27d 12m 35.144s	2.33	26.04±0.02	25.65±0.03	0.38±0.03
DFX1	13h 01m 15.569s	+27d 12m 39.320s	4.16	26.73±0.03	26.39±0.06	0.40±0.05
DFX1	13h 01m 15.702s	+27d 12m 37.737s	1.63	26.85±0.03	26.41±0.06	0.50±0.05
DFX1	13h 01m 16.090s	+27d 12m 36.765s	4.36	26.90±0.03	26.48±0.06	0.46±0.05
DFX1	13h 01m 15.731s	+27d 12m 35.464s	1.85	26.86±0.03	26.57±0.07	0.48±0.05
DFX1	13h 01m 16.206s	+27d 12m 49.881s	14.25	27.12±0.04	26.64±0.07	0.35±0.07
DFX1	13h 01m 15.890s	+27d 12m 37.688s	1.51	27.12±0.04	26.65±0.07	0.52±0.06
DFX1	13h 01m 16.010s	+27d 12m 32.522s	5.47	27.41±0.05	26.75±0.08	0.41±0.08
DFX1	13h 01m 15.775s	+27d 12m 31.074s	5.93	27.03±0.04	26.76±0.08	0.36±0.06
DFX1	13h 01m 16.374s	+27d 12m 47.035s	13.22	27.29±0.05	26.78±0.08	0.43±0.07
DFX1	13h 01m 15.843s	+27d 12m 38.150s	1.32	27.13±0.04	26.81±0.09	0.48±0.06
DFX1	13h 01m 15.823s	+27d 12m 47.546s	10.55	27.21±0.04	26.98±0.10	0.43±0.07
DFX1	13h 01m 15.864s	+27d 12m 32.869s	4.24	27.49±0.05	27.01±0.10	0.44±0.09
DFX1	13h 01m 15.461s	+27d 12m 37.514s	5.10	27.37±0.05	27.06±0.11	0.41±0.08
DFX1	13h 01m 16.154s	+27d 12m 40.703s	6.47	27.61±0.06	27.06±0.10	0.40±0.10
DFX1	13h 01m 15.623s	+27d 12m 27.205s	10.14	27.87±0.07	27.27±0.12	0.71±0.10
DFX1	13h 01m 15.751s	+27d 12m 41.295s	4.35	27.84±0.07	27.29±0.13	0.37±0.12
DFX1	13h 01m 15.403s	+27d 12m 37.138s	5.94	27.97±0.08	27.41±0.14	0.41±0.13
DFX1	13h 01m 15.313s	+27d 12m 40.390s	8.04	27.75±0.07	27.41±0.14	0.48±0.11